TÉCNICO LISBOA

Unsteady behaviour of helicopter blades

Francisco Baptista Romão Machado

Thesis to obtain the Master of Science Degree in

Mechanical Engineering

Supervisors: Prof. Filipe Szolnoky Ramos Pinto Cunha

Prof. José Maria Campos da Silva André

Examination Committee

Chairperson: Prof. Carlos Frederico Neves Bettencourt da Silva

Supervisor: Prof. José Maria Campos da Silva André

Member of the Committee: Prof. Luís Rego da Cunha de Eça

February 2021

Acknowledgments

I would like to thank Professor Filipe Cunha and Professor José Maria André for the number of hours they have spent on me and for all their help. They were tireless and for that, thank you.
To Professor José Chaves Pereira, for helping me with the meshing and the software, thank you.
I would like to thank Professor Luis Eça. His inputs regarding the turbulence models and the validation of results were very helpful.

Abstract

This work aims at investigating the dynamic stall characteristics of a NACA 0012 airfoil, at different conditions. The objective was to obtain concrete results on how dynamic stall really differs from static stall, in terms of lift overshoot, nose-down pitching moment and vortex formation, on the upper surface.

In order to accomplish these objectives, CFD simulations were performed using *Star-CCM+*. RANS coupled with transition model $\gamma - Re_\theta$ was used in all the performed simulations. For steady stall study, the airfoil AoA changed and allowed the identification of pre-stall AoA, stall AoA and post-stall AoA for a specific Re. Furthermore, information regarding maximum C_l, C_d behaviour and C_m break at stall was gathered. For the dynamic case, a different method was implemented. The airfoil was static and at null AoA, with the flow coming from the bottom and left boundaries reaching the airfoil with some AoA determined by the pitching motion of each dynamic case.

To provide a clear study of dynamic stall, given the different regimes of it, two different cases were studies: light stall and deep stall. The deep stall case is of course the critical case, with very high AoA and strong vortex shedding across the upper surface of the airfoil. In addition, studies on the influence of reduced frequency and Reynolds number on this phenomenon were performed.

Keywords: Dynamic stall, Retreating blade stall, Helicopter, Dynamic stall vortex, CFD

Resumo

Este trabalho teve como foco o estudo das características da perda de sustentação dinâmica num perfil NACA 0012, em diferentes condições. O objetivo foi obter resultados concretos no que toca às diferenças entre a perda de sustentação dinâmica e a perda de sustentação estática, em termos do aumento da sustentação, momento de picada negativo e a formação de vórtices no extradorso.

De modo a concretizar o objetivo da tese, simulações *CFD* foram realizadas com o programa *Star-CCM.* O modelo de turbulência $k-\omega$ SST juntamente com o modelo de transição $\gamma - Re_\theta$ foi utilizado em todas as simulações. Para o estudo da perda de sustentação, o ângulo de ataque do perfil foi variado, permitindo a identificação de situações de pré-perda, perda e pós-perda de sustentação, para um Re específico. Informação referente a valores máximos de C_l, C_d e C_m foram obtidas. Para o caso dinâmico, um método diferente foi implementado. Neste caso, o perfil foi mantido estático e a zero graus, com o fluido proveniente das fronteiras de baixo e esquerda a atingir o perfil com determinado ângulo de ataque, de acordo com equação do movimento de picada de cada caso.

De modo a fornecer um estudo claro sobre o caso dinâmico, dados os diferentes regimes do mesmo, dois casos dinâmicos diferentes foram estudados: perda de sustentação dinâmica suave e perda de sustentação dinâmica forte. O último trata-se de um caso crítico, com ângulos de ataque elevados e forte libertação de vórtices ao longo do extradorso do perfil. Para além destes estudos, foi também estudada a influência da frequência reduzida e do número de Reynolds neste fenómeno.

.

Palavras-chave: Perda de sustentação dinâmica, CFD, Helicóptero

Table of Contents

List of figures

List of Tables

Nomenclature

Greek symbols

α	Angle of attack
$\bar{\alpha}$	Mean angle of attack
$\tilde{\alpha}$	Amplitude of the angle of attack
$\dot{\alpha}$	Time rate change of the angle of attack
α_{max}	Maximum angle of attack
δ	Boundary layer thickness
δ_{ij}	Kronecker delta
δ_{RE}	Numerical error estimation
Δy_1	Near Wall prism layer thickness
ϵ	Turbulent dissipation
γ	Intermittency
κ	Reduced frequency
Λ	Sweep angle
μ	Molecular viscosity coefficient
μ_τ	Eddy viscosity
ν	Kinematic viscosity
ν_t	Kinematic eddy viscosity
ω	Specific turbulent dissipation rate
ϕ	Induced angle of attack
Φ	Local flow quantity
ρ	Density
τ_{ij}	Reynolds stress tensor

τ_w Wall shear stress

θ Pitch angle

ψ Azimuth angle

Roman symbols

a Speed of sound

c Chord

C_l Lift coefficient

C_d Drag coefficient

C_m Pitching moment coefficient about $0.25c$

C_p Pressure coefficient

C_f Skin friction coefficient

d Diameter

D Drag

$D_{pressure}$ Pressure drag

e_{rel} Relative error

f Vortex shedding frequency

F Resultant force

Fs Safety Factor

h_i Number of cells of mesh i

I Turbulence intensity

k Turbulent kinetic energy

L Lift

M Mach number

Re Reynolds number

Re_θ Momentum thickness Reynolds number

r_i Grid refinement ratio of mesh i

St	Strouhal number
S_{ij}	Strain-rate tensor
t	Time
T	Thickness
u_i	Velocity components
u_τ	Friction velocity
U_∞	Flow Velocity
U_x	Velocity in the x direction
U_y	Velocity in the y direction
U_{num}	Numerical Uncertainty
U_R	Radial velocity
U_T	Normal velocity
w	Angular frequency
y^+	Dimensionless wall distance

Acronyms

2D	Two dimensions
3D	Three dimensions
AoA	Angle of Attack
BET	Blade Element Theory
BL	Boundary Layer
BSL	Baseline Model
CFD	Computational Fluid Dynamics
CFL	Courant Number
DSV	Dynamic Stall Vortex
LE	Leading Edge
LEV	Leading Edge Vortex
MAV	Micro-Air Vehicle
RANS	Reynolds Averaged Navier-Stokes
SA	Spalart-Almaras Model
SST	Shear Stress Transport
TE	Trailing Edge
TEV	Trailing Edge Vortex

Chapter 1

Introduction

1.1 Motivation

It is the goal of engineering to not only seek improvement, but also to achieve the maximum efficiency in everything. In aerodynamics and aircraft performance, it is not different. Rotary wings present a different set of problems and difficulties, compared to fixed wings. One of these limiting factors is dynamic stall. Helicopters, wind turbines and Micro-Air Vehicles (MAV) design have been greatly influenced by it.

A helicopter is a very particular flying vehicle, in the sense that it is designed to perform diverse manoeuvres some other aircrafts cannot, such as hovering, sideward, forward, rearward and translations on a vertical axis. In a traditional helicopter configuration, the main rotor is the main responsible for lift production and propulsive forces. The tail rotor is mainly used for yaw motion control.

The blade position can be defined in terms of an azimuth angle, ψ, which is defined as zero when the blade is pointing downstream. In hovering flight, the simplest case, the velocity variation along the blade is azimuthally axisymmetric and radially linear [3]. For forward flight complications arise. It is illustrated in Figure 1 the distribution of incident velocity normal to the leading edge of the rotor blade. The distribution of velocity along the blade remain linear, however, it is no longer axisymmetric with respect to ψ and varies in magnitude.

For forward flight, there is a component of U_∞ that subtracts or adds to the rotational velocity at each part of the blade.

One can easily understand that the advancing side experiences increased velocity while the retreating side experiences decreased velocity. This leads to dissymmetric lift force, and to overcome this problem, the AoA of each blade needs to be different (see Figure1). The AoA of the retreating blade must be increased, while the advancing blade must operate at a lower AoA. If the retreating blade AoA is too high, retreating blade stall can occur, with the helicopter not only losing lift and increasing its pitching moment, but also restricting its forward flight speed, as well as high torsional loads and vibrations on the rotor blades [4], [5].

This time rate of change of the AoA, $\dot{\alpha}$, leads to dynamic stall, a phenomenon that defines overall lifting, propulsive and aeroelastic performance limits of a helicopter rotor.

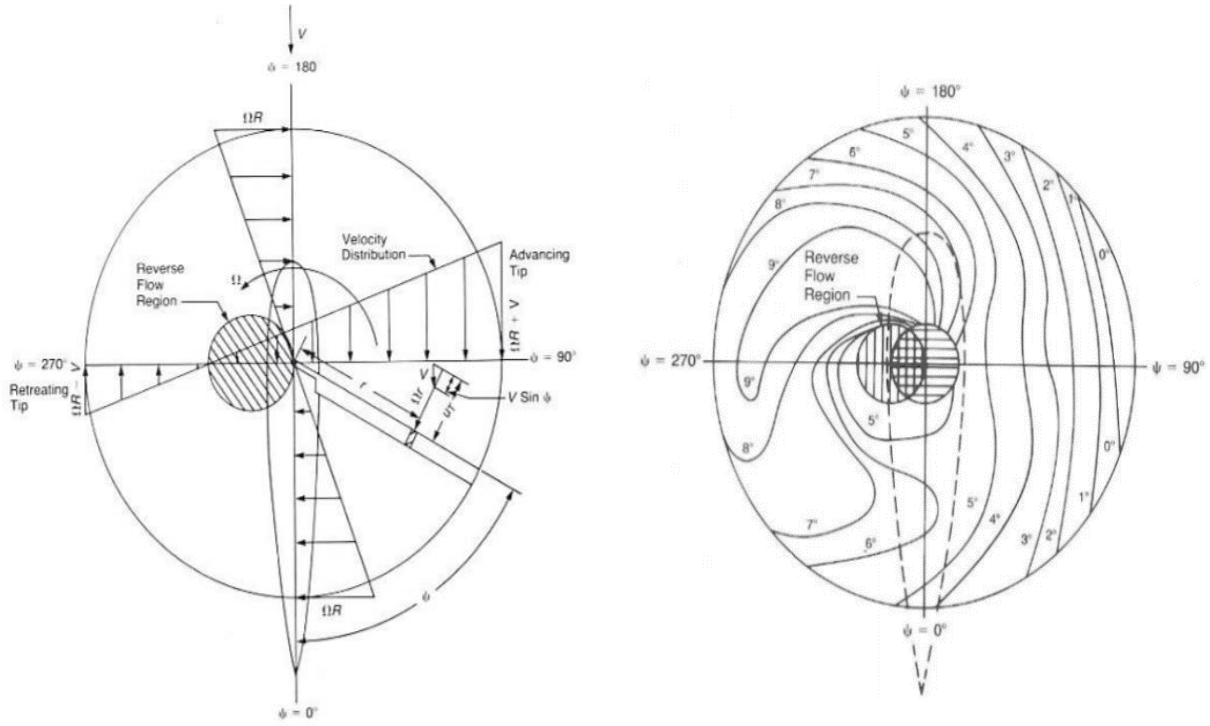

Figure 1: Velocity and AoA distribution for a helicopter blade in forward flight [57]

The overall complexity of the flow structure on a helicopter is considerably higher when compared with fixed-wing aircrafts, mainly due to individual wakes trailed from each blade. In the case of a fixed-wing aircraft, the wing wake and tip vortices trail downstream of the aircraft. For a helicopter in forward flight, blade tip vortices remain close to the rotor and to following blades, close enough to produce a strongly 3D induced velocity field [3]. Additionally, as following blades encounter this induced velocity field, fluctuating airloads are produced, which can be a source of high rotor vibrations and obstructive noise.

At higher forward flight velocities, blade tips on the advancing side can start to penetrate into supercritical and transonic flow regime, leading to compressibility zones, and ultimately, shock waves. Wave drag increases and shock induced flow separation can occur, both leading to a much higher power requirement to drive the rotor. Figure 2, below, presents a schematic of the flow structure and some aerodynamic problem areas on a helicopter in forward flight [3].

Since the 1960's countless studies and experiments have been performed to fully understand the phenomena. In some cases, to mitigate it, and in others, to take advantage of it, like the birds do. The interest to study dynamic stall has been revamped recently, due to the development of MAV, in order to exploit the high magnitudes of the produced lift force.

Still, sixty years have passed and dynamic stall remains one of the major unsolved problems in aerodynamics. What if engineers could take advantage of it? What changes could one see in helicopter's design?

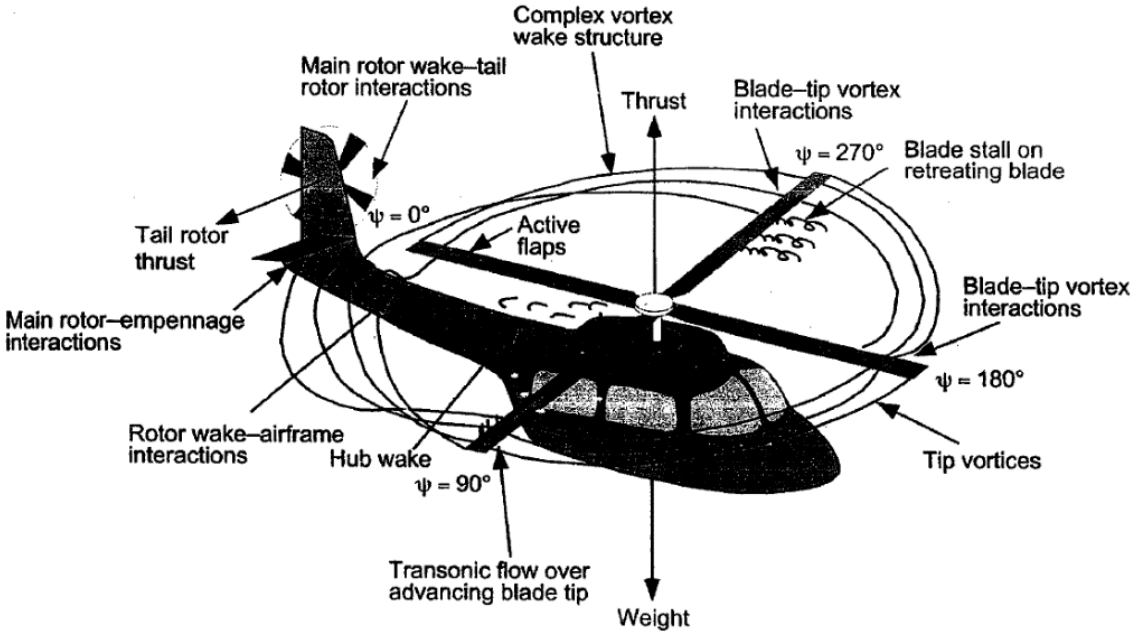

Figure 2: Flow structure around a helicopter in forward flight [3]

1.2 State of the art

The unsteady effects associated with quick changes of the angle of attack of an airfoil, were first observed by Kramer [6]. At the time, there was no perceived applicability, so, very little attention was given to it, up until the 1950's, when it was observed in helicopter's retreating blade [7] [8] [9]. From these works, the stall flutter mechanism of negative damping or moment variation, so that energy is extracted from the fluid was deduced. In the late sixties and early seventies, renewed attention was given and some of the most crucial works came from this period.

Ham [10], Crimi [11], Carta [12], Ericcson [13], McCroskey [14] and others, were on the forefront of these studies. Carta [12] used an energy approach and data from his own tests on 2D oscillating airfoils to study the stall flutter of rotor blades.

Ericcson [13] utilized a quasi-steady approach and the concept of "Moving Wall effect" and caused some controversy among experts, reason why that approach is not followed nowadays. Crimi [11] determined, numerically, the separation points in the boundary layers on 2D airfoils, using a panel method to model the evolution of the wakes. Ham [10] studied analytically the discrete vortices shedding from both the LE and TE. He also conducted some studies on stall flutter [15]. McCroskey [14] and Carr [16] provided information of flow properties leading to leading-edge stall and trailing-edge stall. Freymuth [17] presented flow visualizations using innovative vortex tagging technique. Koochefsahani et al. [18] and Acharya & Metwally [19], through flow visualization experiments, gathered information about surface vorticity flux and effects on pitching acceleration. McCroskey et al. [20] conducted studies on NACA 0012. Varying the leading edge of the profile, three different types of dynamic stall were produced (onset, light and deep stall).

Recently, newfound interest stemming from the study of birds and insects flight has led to a greater number of studies on the topic. Wing area and aspect ratio of birds and insects is generally too small, in comparison to bodyweight, to sustain reasonable steady-state flight [21]. It is believed they take advantage of the unsteady lift, from dynamic stall, to fly [22].

Flying animals' high manoeuvrability, has drawn attention to this type of stall due to its potential applicability on fighter jets. Furthermore, Micro-Air Vehicles, have also increased the need of understanding dynamic stall, to exploit the high magnitude of the lift force produced.

1.3 Objectives

Owing to the importance of differentiating steady stall from dynamic stall, the present work evaluates, using CFD simulations as a tool, the differences in the aerodynamic coefficients and flow phenomena between steady stall and dynamic stall of an airfoil NACA 0012. For that, RANS turbulence model $k-\omega$ SST coupled with transition model $\gamma - Re_\theta$ was chosen.

The detailed objectives of the present thesis are the following:

- Evaluate how refined must be the mesh in order to properly model steady stall, also in accordance with the available computational power.
- Using the chosen mesh, evaluate light dynamic stall case and how the aerodynamic coefficients are affected, in comparison with steady stall.
- Evaluate deep dynamic stall case and provide information about the DSV formation on the upper surface and how it affects lift overshoot and nose-down pitching moment, in comparison with steady stall and light dynamic stall.
- Identification of the importance of reduced frequency in dynamic stall and how increasing it changes aerodynamic coefficients and flow separation.
- Evaluate if Re is a major parameter when studying dynamic stall, for high Re cases.

1.4 Thesis outline

The first chapter contains the introduction and motivation to the subject. The objectives of this work are also presented. The second chapter is the theoretical background of static stall and dynamic stall. Turbulence modelling is also presented. The third chapter contains the mathematical formulation of the applied models in this thesis, RANS, $k-\omega$ SST coupled with transition modelling $\gamma - Re_\theta$. Chapter four explains the CFD methodology adopted. Chapter five presents the results and their analysis. Chapter six presents the conclusions and future work is also proposed.

Chapter 2

Background

Before tackling the issue of dynamic stall, particularly on a pitching airfoil, some concepts must be understood. First, stall will be thoroughly discussed, both static and dynamic stall. After it, a brief introduction and main concepts of CFD, will be presented.

2.1 Static Stall

At high AoA, intense adverse pressure gradients on the upper surface of the airfoil, produce massive separations, which results in lift loss and a great increase in drag force [2]. The AoA at which this occurs is called critical angle of attack. This phenomenon is caused by flow separation and can be divided in three different types, as stated by McCullough *et al.* [23]: Trailing Edge stall, Leading Edge stall and Thin-airfoil stall.

TE stall is typical of thick airfoil profiles, $t/c > 12\%$. As the AoA increases, suction peak on the upper surface increases and moves towards the LE. Due to that, adverse pressure gradient occurs "earlier", and that leads to transition occurring earlier also. Subsequently, the turbulent boundary layer (BL) develops in an increasingly adverse pressure gradient; as the AoA continues to increase, the turbulent BL ends up separating at the TE. Continuing to increase the AoA, separation point moves upstream (towards the LE), and in consequence, $\frac{dC_L}{d\alpha}$ decreases until stationarity and eventually, with further increases in AoA, becomes negative.

For thin-airfoils, $t/c < 9\%$, any positive AoA different than zero, leads to a strong suction peak and adverse pressure gradient on the LE. Therefore, flow reaches the LE in laminar regime (consequence of the strong favourable pressure gradient encountered on the bottom surface), meaning that transition will occur during separation; at small AoA, by Coanda effect, flow reattaches originating a small separation bubble. At some higher AoA, this is no longer possible, the bubble bursts with reattachment occurring downstream (close to the TE), giving origin to a longer bubble. The airfoil is stalled, typically, when the bubble reattaches close to the TE.

Intermediate airfoils $9\% < t/c < 12\%$, which have a softer LE curvature than thin-airfoils, are similar to the case in the above paragraph. However, there is no bubble bursting until higher AoA; but when it bursts, it occurs without being able to reattach, which leads to an abrupt lift loss. This type of stall is designated LE stall.

There are airfoils, for example like the, well-known, NACA 0012 placed in between the limits of two stall regimes (for the aforementioned airfoil, it will be between the thick and intermediate interval).

This type of stall is called mixed stall [2], meaning, depending on the airfoil geometry, Re or roughness, the airfoil might initially have one type of stall and progresses to other as the Re changes, for example.

To achieve the goals of this work, it will be explored the NACA 0012 case. At small AoA, a short separation bubble form near the LE, followed by turbulent boundary layer. At smaller Re, the turbulent boundary layer separates closer to the TE, and it progresses towards the LE. This leads to TE stall, despite what the short bubble might lead us to think. However, for larger Re (for example, 10^6) the turbulent boundary layer does not separate and stall occurs not only at larger AoA, but also due to the bubble burst. In this case, LE stall.

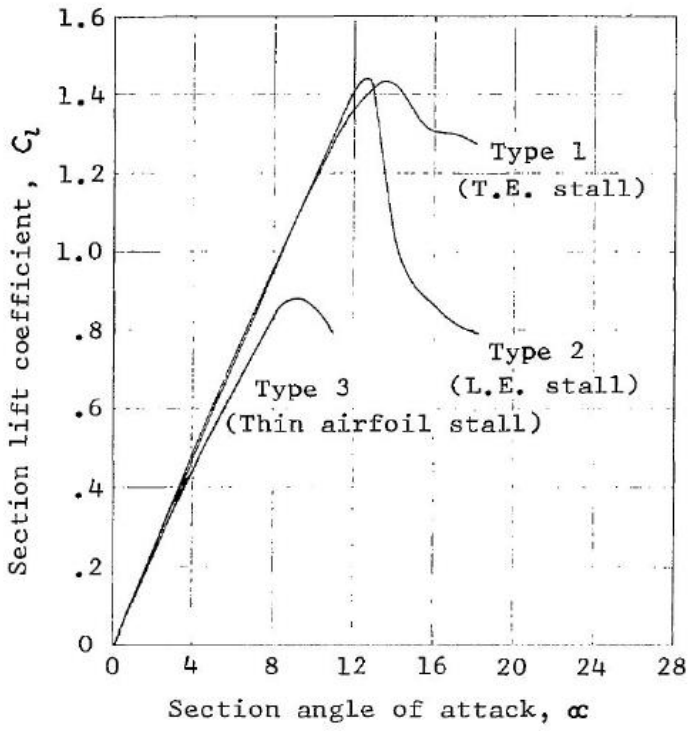

Figure 3: Representative lift curves for different types of stall [58]

2.2 Dynamic Stall

Dynamic stall will occur on any airfoil or lifting surface when it is subjected to time-dependent pitching, plunging, heaving or vertical translation, that takes the effective AoA above its static stall angle [3]. This type of stall is distinguished by a delay in the onset of flow separation, to higher AoA, then would occur statically. This delay can lead to better performance as well as operational flight envelope, as long as separation does not occur. When separation occurs, dynamic stall may become a real danger.

As an airfoil pitches-up, separation point on the upper surface moves upstream, a free shear layer wake forms at the TE and a net positive (counter-clockwise) vorticity is shed into the wake [24] (see Figure 4). As the AoA increases, the separated region on the upper surface rolls-up (reverse flow), as it comes closer to the vicinity of the LE. As the region of reverse flow moves upstream, catastrophic breakdown of the separation bubble near the leading edge occurs, originating the primary vortex (also

called, dynamic stall vortex, DSV) and shortly after it, occurs the pitching moment break (moment stall), due to the additional suction over the upper surface.

Shortly after maximum AoA is attained, the vortex detaches and continuous its movement downstream. The passage of this vortex across the suction side of the airfoil induces a moving pressure wave, which provides additional vortex lift and the consequent dislocation of the center of pressure originates strong nose down pitching moment. During the same time, the free shear layer wake grows in intensity and can roll up to form a counterclockwise trailing edge vortex (TEV).

As the airfoil starts to pitch down, DSV moves further downstream and separation point moves backwards, towards the TE. Thus, full separation state over the upper surface and consequent abrupt lift loss (lift stall). Shortly after the downwards pitching movement has begun, TEV detaches and drifts downstream. For some cases, at some lower AoA, flow reattaches, returning to pre-stall conditions. Hence the particular hysteresis on aerodynamic loads as a function of AoA plots, as shown by Figure 4.

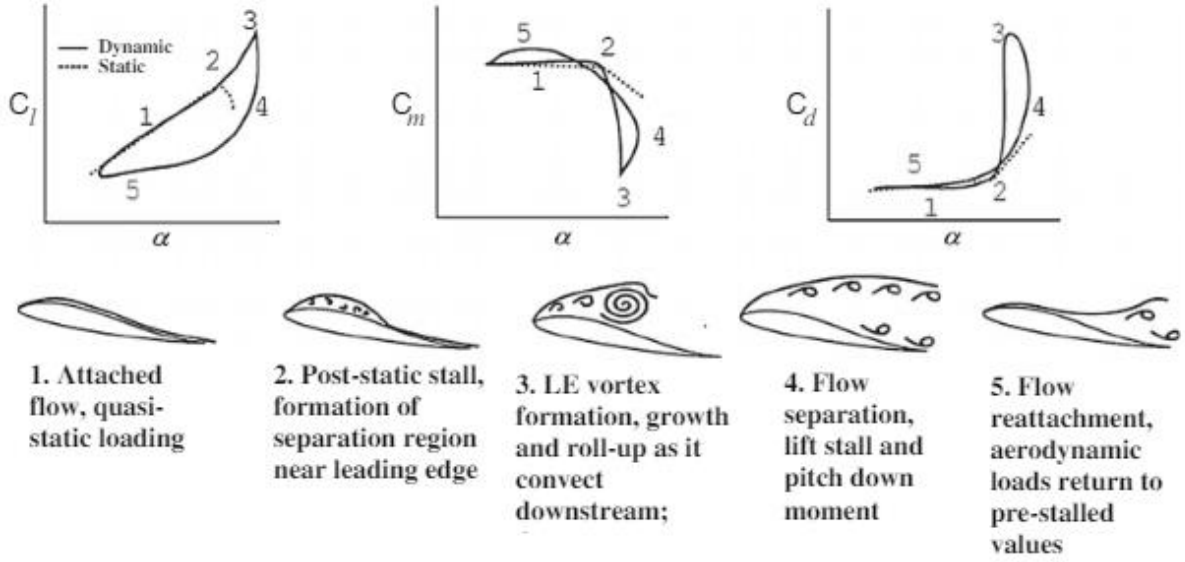

Figure 4: Typical dynamic stall aerodynamic coefficients and flow structure evolution [53]

2.3 Factors that affect dynamic stall behaviour

2.3.1 Reduced Frequency, κ

The reduced frequency is used to describe the unsteadiness of flows over airfoils and wings [25]. It is defined as the ratio of convective time scales ($^{c}/_{U_\infty}$) and the time scale of forced oscillation ($^{1}/_{\dot{\alpha}}$). It can be shown that the reduced frequency appears when nondimensionalizing the Navier-Stokes equations, or alternatively, using dimensional analysis for a resultant force F on an airfoil of chord c, oscillating at angular frequency w in a flow of velocity U_∞:

$$\frac{F}{\rho U_\infty^2 c^2} = f\left(\frac{\rho U_\infty c}{\mu}, \frac{U_\infty}{a}, \frac{wc}{U_\infty}\right) = f(Re, M, k) \tag{2.1}$$

For an airfoil of chord length of c, pitching about the mid-chord at a constant pitch rate of $\dot{\alpha}$ (rad/s), the reduced frequency is defined as [26]:

$$\kappa = \frac{c\dot{\alpha}}{2U_\infty} \tag{2.2}$$

Thus when $\kappa \sim 1$, the convective and unsteady time scales are of the same order of magnitude and the flow is unsteady. However, significant differences compared to the static stall characteristics have been observed for reduced frequencies as low as 0.05 [27] To better understand why these differences occur, Digavalli [24] proposed to analyse the ratio between viscous diffusion time scale and the airfoil motion time scale, $\kappa \mathrm{Re}_c$. The ratio corresponding to length scales is then $\kappa\sqrt{Re_c}$. For $\kappa \sim 0.01$, both the above ratios are higher than 1.0, making the flow unsteady from a viscous perspective. Experiments conducted in [28] illustrated that unsteady effects manifested at reduced frequencies as low as 0.005. For this value of κ, no clear peaks in lift resulting from DSV were observed, yet, there were clear increases in both the critical AoA and the lift force produced, Figure 5. It has to be emphasized that in various cases $\kappa\sqrt{Re_c}$ will be larger than unity, due to high Reynolds numbers used nowadays in aerospace applications, hence even small disturbances can cause great unsteadiness in blades and wings.

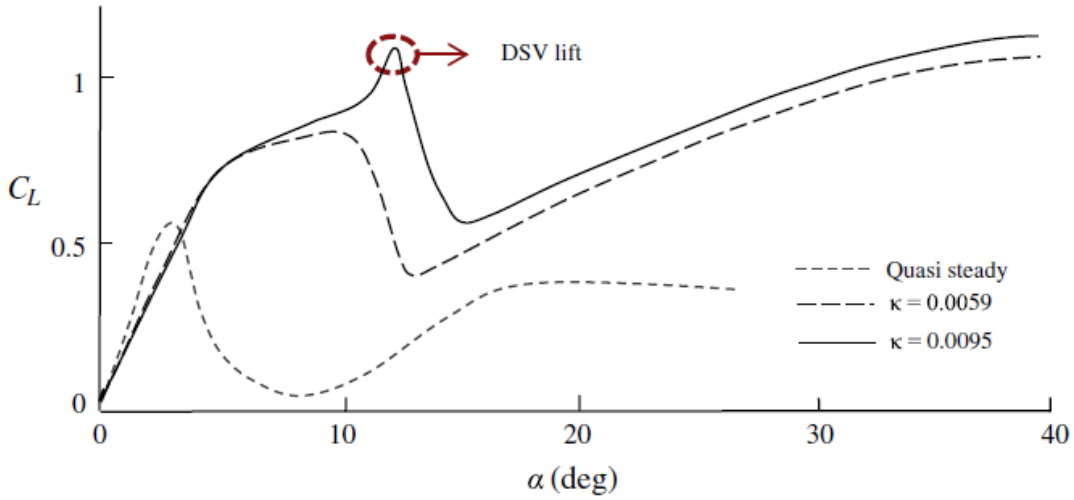

Figure 5: Reduced frequency effect on lift coefficient [28]

The dynamic stall problems encountered more often in practice are the ones involving periodic oscillation of the airfoil (like pitching and heaving), rather than a constant pitch rate. The present work focus on an airfoil pitching sinusoidally, having an instantaneous AoA given by:

$$\alpha(t) = \bar{\alpha} + \tilde{\alpha}\sin(wt) \tag{2.3}$$

where $\bar{\alpha}$ is the mean AoA, $\tilde{\alpha}$ is the amplitude of oscillation and w the frequency of the oscillation. For such pitching motions,

$$\kappa = \frac{wc}{2U_\infty} \tag{2.4}$$

Comparisons with the steady case indicate that for higher reduced frequencies, higher lift force can be produced by the airfoil, beyond the critical AoA, similarly to what can be seen in Figure 5. The onset of dynamic stall is delayed for higher AoA, as the reduced frequency increases, Figure 6.

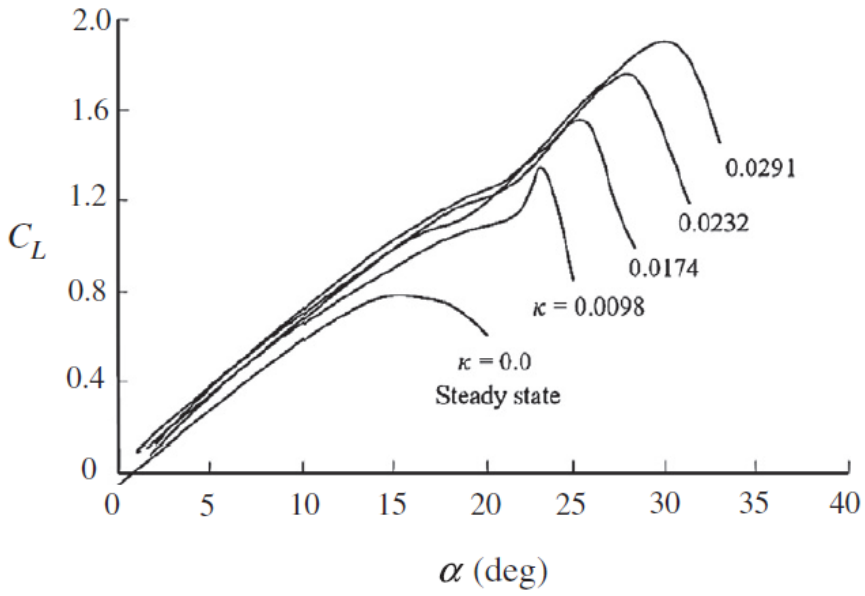

Figure 6: Delay of dynamic stall onset, for various values of κ [28]

2.3.2 Reynolds Number, *Re*

For smaller Reynolds numbers, Robinson and Wissler [29] indicated that as Re increases, the low-pressure peaks near the LE increased. Similarly, Choudhry and Knight [30], concluded that an increase on Re from 10^4 to 10^5 led to the decrease of the length scales associated with the flow structures. Still, both of these studies concluded that Re had no major role in the dynamic stall process as a whole.

The presence of turbulence can lead to different types of separation processes on the upper surface. Regardless the separation process, the separated shear layer rolls-up to form the DSV in all cases, so in that regard, one could say that Re does not affect dynamic stall as a whole. Looking into it in a more detailed and careful manner, Chandrasekhara et al. [31] observed that Re not only increased the peak suction levels, but also delayed dynamic stall to higher AoA and shrank the laminar separation bubble.

For the majority of airfoils at medium-high Re numbers (10^6) stall will be of the type of LE stall [2]. The shear layer goes through transition and becomes turbulent before it reattaches to form the bubble. Further downstream the boundary layer separates again. As the AoA is increased, the bubble has a small growth due to the downstream separation point, while at the same time the turbulent separation point moves upstream.

For Re around transition, the bubble can grow to encompass a larger fraction of the chord (~25%), which not only modifies the overall flow, but also the separation onset and the formation of the DSV.

2.3.3 Mean angle and Amplitude

For the case of periodic motions, such as pitching, $\bar{\alpha}$ and $\tilde{\alpha}$ cannot be completely separated since $\alpha_{\max}$ depends on the sum of both and is important in determining flow separation [1]. McCroskey believed that more important than looking solely to each one of these angles, it would be better to do comparisons when the three parameters, $\bar{\alpha}$, $\tilde{\alpha}$ and w, were selected to match the $\alpha(t)$ history over the portion of the cycle where critical AoA was exceeded.

Figure 7, below, presents the lift coefficient and momentum coefficient for two cases with the same $\alpha_{\max}$ and the same $\tilde{\alpha}\kappa^2$, which is a parameter that McCroskey affirms to have great impact when trying to match different pitching motions.

Moment stall and lift stall match well for both cases and the same goes for the lift overshoot and minimum pitching moment. Differences occur, however, for the downstroke (see dashed lines), leading to the net torsion damping being slightly different for each case and to the lift hysteresis to differ. It is not presented here, but this examination was done by McCroskey for the results obtained in [32] and the reached conclusion, although not clear if is extendable to other types of motion, was that the better the match between $\alpha(t)$ history, the better match between the aerodynamic coefficients [1].

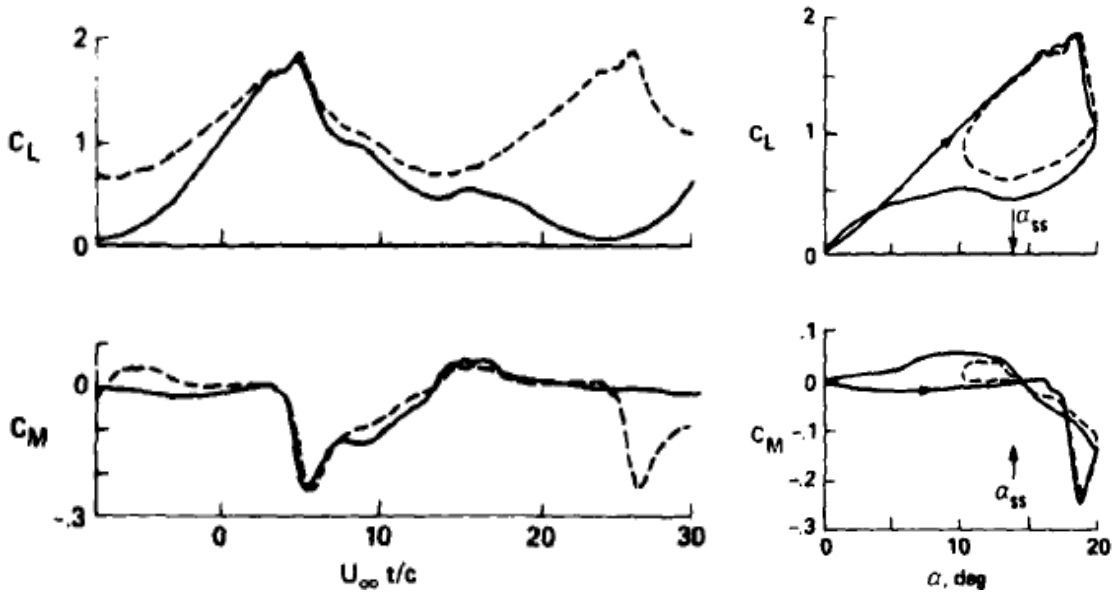

Figure 7: Lift and pitching moment coefficients for two cases with $\alpha_{max} = 20º$.
Solid lines: $\alpha(t) = 10 + 10\,sin(wt)$, $\kappa = 0.1$.
Dashed lines: $\alpha(t) = 15 + 5\,sin(wt)$, $\kappa = 0.15$ [1]

2.3.4 Other parameters

The following parameters were not as important as the previous ones for this work. Still, it is important to understand their effect on dynamic stall, as they might be relevant for future works on the matter.

2.3.4.1 Mach Number, M_∞

When the subsonic freestream Mach number, M_∞ and the AoA are increased beyond certain values, a local region of supersonic flow develops over the airfoil. This supersonic region is usually terminated by a nearly normal shock wave which interacts with the boundary layer. For sufficiently strong shocks, boundary layer separation occurs at the foot of the shock. The disturbances caused by the interaction of the shock and the boundary layer in the separated zone, will propagate upstream, hence the existing normal shock will oscillate leading to buffeting [33]. McCroskey et al. [32] indicated that for airfoils with sinusoidal pitching, sonic conditions were observed for $M_\infty \geq 0.2$.

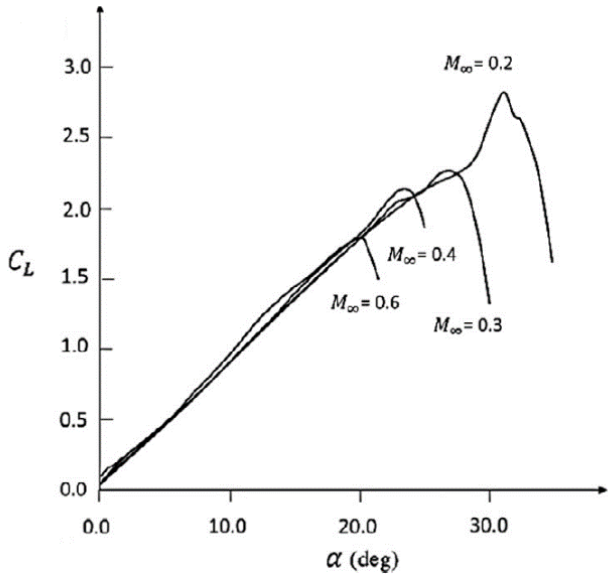

Figure 8: Effects of increasing the Mach number while keeping κ constant (0.0225) on the lift characteristics of NACA 0015 airfoil [28]

Due to severe shock-boundary layer interaction, the separation near the foot of the shock spreads both upstream and downstream, and as it reaches the LE, pressure drops and causes moment stall, with massive flow separations. Regarding lift behaviour of the airfoil, it was observed a decrease in stall delay and in the maximum lift coefficient as M_∞ increases, while keeping both κ and Re constant, as indicated in Figure 8.

2.3.4.2 Airfoil geometry

The shape of the airfoil and its effects on dynamic stall have been studied by McCroskey et al. [1]. It has been believed that the airfoils with better static stall characteristics, have better dynamic stall behaviour, both in terms of maximum lift coefficient and stall delay [3]

Both McCroskey [1] and Leishman [3] concluded that airfoils designed for high static lift capability, should also exhibit a higher AoA capability before stall, when in dynamic conditions. During their studies, the NACA 0012 had a well-rounded pitching moment break, in comparison to most of the other airfoils. This suggested that some TE separation is still present for the NACA 0012, meaning that to some extent, static stall properties may carry over to the dynamic case [3]. Also regarding the pitching moment, NACA 0012 exhibited a much smaller peak (nose down), which could mean a weaker DSV shed for this airfoil.

2.3.4.3 Three-Dimensional effects

The complexity of 3D dynamic stall comes from diverse phenomena, such as wing tip vortices, centrifugal flow caused by the rotation of the blades, interaction with other blades and unsteady separations. The 3D unsteady separating flows are still poorly understood [3].

The unsteady separated flows have been observed to be dominated by large-scale vortical structures [34]. Three dimensionality effects are restricted, primarily, to the regions near the wing tips where the flow can be distinguished as three zones: wing tip vortex, DSV and an intermediate zone where both interact, see Figure 9. The core of DSV is affected by the wing tip vortex in the intermediate zone and remains close to the LE, regardless of the instantaneous AoA. Moreover, the spatial extent of the intermediate zone extends towards the wing's root, as the AoA increases.

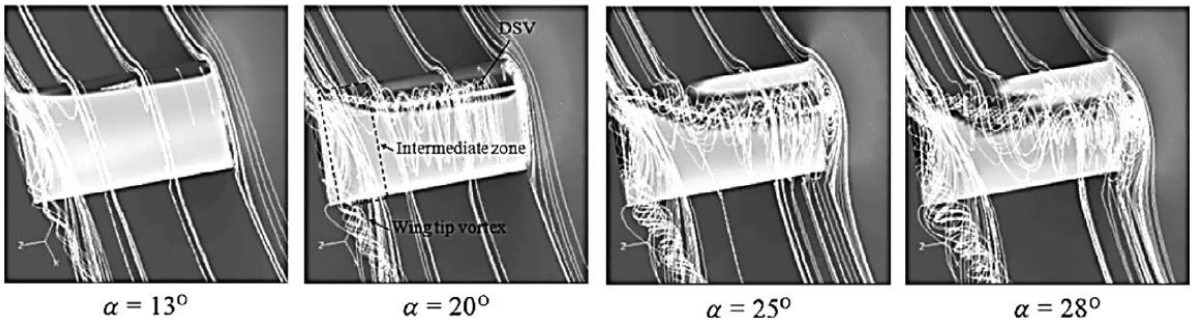

Figure 9: Streamlines around a NACA 0012 profile, pitching at a constant k, indicating the spanwise evolution of the DSV and its interactions with the wing tip vortices [59]

2.3.4.4 Effects of Sweep Angle

The local sweep or yaw angle of the flow to a blade element, can be significant in forward flight. The sweep angle, Λ, is shown in Figure 10 and is defined as [3]:

$$\Lambda = tan^{-1}\left(\frac{U_R}{U_T}\right) \tag{2.5}$$

with U_R being the radial velocity and the normal component being U_T.

Usually, in the classical blade element theory, BET, the effect of sweep on aerodynamic forces is neglected [35]. However, when an airfoil is operated near its critical AoA, this may not be a valid assumption, as seen in Figure 10.

The unsteady $\Lambda = 30º$ shows a delay in lift stall to a higher AoA but, contrary to the static case, there is not a significant increase in the attainable lift force (or coefficient). Moreover, a narrower hysteresis is obtained for the sweep angle case, with the mean lift value also being higher.

For the pitching moment coefficient, moment stall occurs for the same AoA in both cases and, interestingly, the minimum pitching moment for the $\Lambda = 30º$ occurs to a higher AoA, with a less steep curve. This suggests that the velocity at which the shedding of DSV over the chord occurs, is lower.

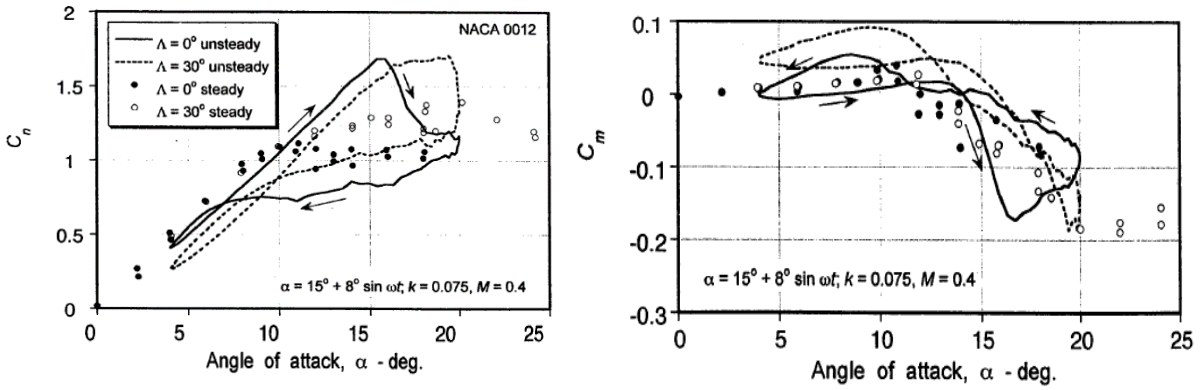

Figure 10: Sweep angle effect on airloads of NACA 0012 pitching [3]

2.4 Computational Fluid Dynamics (CFD)

2.4.1 Overview of CFD

In the middle of the 19th century Euler's equations for inviscid flows and Navier-Stokes equations for viscid flow were already established. Yet, they could not be solved because of their system of non-linear partial differential equations. The only approach was to make (several) assumptions and simplifications. In the 1970s, however, the introduction of CFD was revolutionizing fluid dynamics.

It all began way before that, with L.F. Richardson [36], when he first introduced a finite difference technique for numerical solution of Laplace's equation. In 1928, Courant-Friedrichs-Lewy (CFL) defined stability criterion for the numerical solution of hyperbolic partial differential equations [37]. Professor John Von Neumann evaluated the stability of numerical methods in order to solve time-marching problems [38]. Many more contributed during this time and, most of them, were focused on solving the Riemann problem [39]. All of them and many more contributed to the beginning of CFD.

2.4.2 Turbulence modelling

Turbulence requires a statistical approach due to its random fluctuations. Reynolds introduced a procedure in which all quantities could be expressed as a sum of their mean and fluctuating parts, the RANS (Reynols-Averaged-Navier-Stokes) equations. This comes at a price, the so-called closure problem. Chapter 3 takes a closer look at Navier-Stokes equations and RANS, but for now, let us say that turbulence models are constitutive equations that predict the statistical evolution of turbulent flows [40]. Some mathematical models are: RANS models, Unsteady RANS (URANS), Detached-Eddy

Simulation (DES), Large-Eddy simulation (LES) and Direct Numerical Simulation (DNS). In the present work, greater focus will be given to RANS models.

In 1997, Spalart proposed a new approach named DES [41], which is a hybrid model created to treat turbulence of separated flows at any Reynolds number and at the same time overcome the computational constraints of LES and DNS. In short, it can be explained as a combination of RANS in the boundary layer and LES in the separated regions.

2.4.3 CFD approach in the present work

For the purpose of this work, RANS was chosen and in order to obtain the flow separation patterns on the upper surface of the airfoil, the turbulence model $k-\omega$ SST (Menter) was used.

The choice of RANS was straightforward, since it is a 2D study and not only time, but computational power were major constraints. In terms of the $k-\omega$ SST model [42] [43], it is widely used in industry and it was created in order to deal with adverse pressure gradients and flow separation. Menter presented it in 1994 and can be explained as a combination of two previous models: $k-\omega$ and $k-\varepsilon$, with the first being used in the inner region of the boundary layer and the second model applied in the free shear flow. Its mathematical formulation is presented in section 3.2.2**.**

Ultimately, the choice of the turbulence model was between the Spalart-Allmaras (SA) or the $k-\omega$ SST, since both give the best prediction of dynamic stall out of the RANS turbulence models [44]. SA obtained reasonable agreement with the measured lift and pitching moment hysteresis but failed to predict the drag increase at the end of the upstroke, whereas the $k-\omega$ SST did better predicting it. So, ultimately, $k-\omega$ SST was the chosen turbulence model.

Chapter 3

Mathematical Model

In this section the mathematical models applied in the present work are presented. First, as any aerodynamics or fluid dynamics work does, Navier-Stokes and RANS equations will be presented, to better understand the closure problem of RANS. Following this with a mathematical explanation of the two-equation turbulence model $k-\omega$ SST and the transition model $\gamma - Re_\theta$.

3.1 RANS Equations

The motion of a fluid is described by the Navier-Stokes equations. Assuming incompressible flow with constant viscosity, the Navier-Stokes equations are written as two partial differential equations. These represent the mass conservation – continuity equation – and the momentum conservation for an infinitesimal control volume, which in Einstein notation are:

$$\frac{\partial u_i}{\partial x_i} = 0 \tag{3.1}$$

$$\frac{\partial u_i}{\partial t} + u_j \frac{\partial u_i}{\partial x_j} = -\frac{1}{\rho}\frac{\partial p}{\partial x_i} + \nu \frac{\partial^2 u_i}{\partial x_j \partial x_j} + f_i \tag{3.2}$$

Where t is the time, u_i are the Cartesian velocity components, ρ is the density of the fluid, p is the static pressure, ν is the kinematic viscosity of the fluid and f_i is the vector of external body forces, per mass unit, in the i direction.

Assuming now that the external body forces are only due to the gravitational field and choosing the local hydrostatic pressure as the reference, the vector of external body forces f_i cancels out and the momentum conservation equations may be written as,

$$\frac{\partial u_i}{\partial t} + u_j \frac{\partial u_i}{\partial x_j} = -\frac{1}{\rho}\frac{\partial P}{\partial x_i} + \nu \frac{\partial^2 u_i}{\partial x_j \partial x_j} \tag{3.3}$$

where P is the relative pressure with the hydrostatic pressure as the reference.

Solving numerically the Navier-Stokes equations for flows at high Reynolds numbers lead to unfeasible computational requirements. To calculate and characterize turbulent flows, and considering their randomness, fluctuating behaviour, a statistical approach can be applied to the above equations.

Reynolds proposed a procedure where all quantities in the Navier-Stokes equations are written as a sum of their steady mean value and of their fluctuating component [45]. This time-averaging method is then applied to the continuity and momentum equations of Navier-Stokes and these are solved for their mean quantities, leading to the Reynolds-Averaged Navier-Stokes (RANS) equations. For incompressible Newtonian fluids are:

$$\frac{\partial \overline{u_i}}{\partial x_i} = 0 \tag{3.4}$$

$$\frac{\partial \overline{u_i}}{\partial t} + \overline{u_j}\frac{\partial \overline{u_i}}{\partial x_j} = -\frac{1}{\rho}\frac{\partial \bar{P}}{\partial x_i} + \nu\frac{\partial^2 \overline{u_i}}{\partial x_j \partial x_j} + \frac{1}{\rho}\frac{\partial}{\partial x_j}(-\rho\overline{u_i' u_j'}) \tag{3.5}$$

where, when compared to Equation 3.3, there is an extra-term at the right-hand side, $-\rho\overline{u_i' u_j'}$. This term may be interpreted, according to Newton's 2^{nd} Law, as a turbulent stress tensor, the Reynolds stress tensor, τ_{ij}.

The trace of Reynolds tensor, τ_{ii} is related to the turbulence kinetic energy, $k = \frac{1}{2}\rho\overline{u_i' u_j'}$ by:

$$\tau_{ii} = -2k \tag{3.6}$$

The "appearance" of τ_{ij} in RANS equations leads to the famous "closure problem". It has more unknowns than equations. Turbulence models are necessary to determine τ_{ij}.

3.2 Eddy Viscosity Models

RANS turbulence models may be divided into two major groups, the Reynolds Stress models and the Eddy Viscosity models. Only the second one will be approached in this document, since it was the one utilized in this work.

3.2.1 Boussinesq Assumption

The Boussinesq assumption [46] is used by several turbulence models, namely algebraic, one-equation and two-equation models. It introduced the concept of eddy viscosity and how momentum transfer caused by turbulent eddies can be modelled with it.

The assumption states that the tensor of the Reynolds stresses, τ_{ij}, can be written as:

$$\frac{\tau_{ij}}{\rho} = 2\nu_t S_{ij} - \frac{2}{3}k\delta_{ij} \tag{3.7}$$

where δ_{ij} is the Kronecker delta, k is the turbulence kinetic energy and S_{ij} is the mean strain-rate tensor, defined as,

$$S_{ij} = \frac{1}{2}\left(\frac{\partial \overline{u_i}}{\partial x_j} + \frac{\partial \overline{u_j}}{\partial x_i}\right) \tag{3.8}$$

3.2.2 Two-Equation Models

Two-equation models solve two separate equations, the turbulent velocity and length scales that are required to define the eddy-viscosity for both a turbulent and a time scale. The two most common and used in the industry are the $k-\varepsilon$ and the $k-\omega$ models (both of them have several forms of the model). For the remaining of this section it considered that $k-\varepsilon$ refers to Standard $k-\varepsilon$, proposed by Launder in 1974 [47].

The first transported variable, k is obviously the turbulence kinetic energy and defines the velocity scale. The second variable depends on the chosen model: ε, the turbulent dissipation or ω, the specific dissipation rate. This variable determines the scale of turbulence.

Let us now focus on the two-equation RANS model used in this thesis, $k-\omega$ SST and how it was developed.

In 1994, Menter [43] introduced the world of CFD to two new two-equation models (empirical models), the $k-\omega$ BSL (baseline model) and the $k-\omega$ SST (shear stress transport). In Menter's own words "the first model utilizes the original $k-\omega$ model of Wilcox in the inner region of the boundary layer and switches to the standard $k-\varepsilon$ in the outer region and in free shear flows (…). The second model results from a modification to the definition of the eddy-viscosity in the BSL model, which accounts for the effect of the transport of the principal turbulent shear stress (…) leads to major improvements in the prediction of adverse pressure gradient flows". This switch between models that Menter refers is performed using a blending function, F_1. The formulation of both models is similar, with only the first set of constants being different.

The definition of $k-\omega$ is then:

$$\frac{D\rho k}{Dt} = \tau_{ij}\frac{\partial u_i}{\partial x_j} - \beta^*\rho\omega k + \frac{\partial}{\partial x_j}\left[(\mu + \sigma_k\mu_t)\frac{\partial k}{\partial x_j}\right] \tag{3.9}$$

$$\frac{D\rho\omega}{Dt} = \frac{\gamma}{\nu_t}\tau_{ij}\frac{\partial u_i}{\partial x_j} - \beta\rho\omega^2 + \frac{\partial}{\partial x_j}\left[(\mu + \sigma_\omega\mu_t)\frac{\partial \omega}{\partial x_j}\right] + 2(1-F_1)\rho\sigma_{\omega 2}\frac{1}{\omega}\frac{\partial k}{\partial x_j}\frac{\partial \omega}{\partial x_j} \tag{3.10}$$

The constants ϕ of the new model are calculated from the constants of set 1, ϕ_1 (SST inner) and constants of set 2, ϕ_2 (standard $k-\varepsilon$) as follows:

$$\phi = F_1\phi_1 + (1-F_1)\phi_2 \tag{3.11}$$

meaning that the constants will change their values between the inner and outer regions, according to the weighting function. As it will be seen right away, these blending functions are null in the far-field and gradually shift, assuming the unitary value at the wall. This way, exactly like Menter proposed, the model vary from $k-\varepsilon$ to $k-\omega$ SST according to the region we are in:

$$F_1 = \tanh(\arg_1^4) \tag{3.12}$$

$$\arg_1 = \min\left[\max\left(\frac{\sqrt{k}}{0.09\omega y}; \frac{500\upsilon}{y^2\omega}\right); \frac{4\rho_{\omega 2}k}{CD_{k\omega}y^2}\right] \tag{3.13}$$

$$CD_{k\omega} = \max\left(2\rho\sigma_{\omega 2}\frac{1}{\omega}\frac{\partial k}{\partial x_j}\frac{\partial \omega}{\partial x_j}, 10^{-20}\right) \tag{3.14}$$

where y is the distance to the next surface and $CD_{k\omega}$ is the positive portion of the cross-diffusion term. As Menter states [43] $\arg_1$ goes to zero far enough away from solid surfaces, because of the dependency on $\frac{1}{y}$ or $\frac{1}{y^2}$ in all terms. As $\arg_1$ goes to zero near the boundary-layer edge, the same happens to F_1 and the standard $k-\varepsilon$ is used in that region.

Moreover, an important definition has to be made, the eddy viscosity:

$$\nu_t = \frac{a_1 k}{\max(a_1\omega; \Omega F_2)} \tag{3.15}$$

where Ω is the absolute value of the vorticity and F_2 is given by:

$$F_2 = \tanh\left(\arg_2^2\right) \tag{3.16}$$

$$\arg_2 = \max\left(2\frac{\sqrt{k}}{0.09\omega y}; \frac{500v}{y^2\omega}\right) \tag{3.17}$$

Table 1: Set 1 $k-\omega$ SST Model constants [43]

σ_{k1}	$\sigma_{\omega 1}$	β_1	a_1	β^*	κ	γ_1
0.85	0.5	0.750	0.31	0.09	0.41	$\frac{\beta_1}{\beta^*} - \frac{\sigma_{\omega 1}\kappa^2}{\sqrt{\beta^*}}$

Table 2: Set 2 $k-\varepsilon$ Model constants [43]

σ_{k2}	$\sigma_{\omega 2}$	β_2	β^*	κ	γ_2
1.0	0.856	0.0828	0.09	0.41	$\frac{\beta_2}{\beta^*} - \frac{\sigma_{\omega 2}\kappa^2}{\sqrt{\beta^*}}$

3.2.3 Transition Modelling

It is important to understand why modelling transition is so difficult. One could say that it arises from its non-linearity, wide range of scales at play, and the different mechanisms that make it occur. Natural transition occurs when the freestream turbulence level is low and Tollmien-Schlichting waves grow and become unstable, leading to turbulent spots which erupt into a fully turbulent regime ($I < 1\%$). When the freestream turbulence intensity is high ($I > 1\%$), bypassing of the first stages of natural transition occurs, and the referred turbulence spots are produced because of freestream disturbances – bypass transition. Separation induced transition ensues when an adverse pressure gradient causes a laminar boundary layers to separate; in the separated shear layer, as already seen in Section 2.1**,** transition can occur and the flow becomes turbulent, occasionally reattaching due to the increased mixing capability of the flow – originates laminar separation bubble.

Several approaches in order to model this phenomenon have been employed, many of them based on different concepts. One common approach, however, is to make use of empirical correlations along with a transport equation for intermittency. This γ is defined as the fraction of time that a given point of the flow is turbulent: γ is zero for laminar flow and one for turbulent flows. The model, although, invokes non-local quantities, like the momentum thickness Reynolds number, Re_θ.

With the full model only released three years later, in 2006, Langtry alongside Menter, [48] proposed a new alternative based on γ, the $\gamma - Re_\theta$ model, which avoids the use of non-local quantities. Two additional transport equations are solved: one for γ and another for the transition onset Reynolds number, coupled with $k-\omega$ SST model. The two transport equations are as follows:

$$\frac{D\rho\gamma}{Dt} = P_\gamma - E_\gamma + \frac{\partial}{\partial x_j}\left[(\mu + \frac{\mu_t}{\sigma_f})\frac{\partial \gamma}{\partial x_j}\right] \tag{3.18}$$

$$\frac{D\rho\tilde{R}e_{\theta t}}{Dt} = P_{\theta t} + \frac{\partial}{\partial x_j}\left[\sigma_{\theta t}(\mu + \mu_t)\frac{\partial \tilde{R}e_{\theta t}}{\partial x_j}\right] \tag{3.19}$$

where γ is the intermittency, $\tilde{R}e_{\theta t}$ is the local transition momentum thickness Reynolds number, P_γ and E_γ are the production and destruction terms of the intermittency equation, while $P_{\theta t}$ is the source term of the transition momentum thickness Reynolds number transport equation. σ_f and $\sigma_{\theta t}$ are constants and the full model can be found in [49].

A phenomenon discussed in [50] may have an impact when using the $\gamma - Re_\theta$ model. Turbulence decay has a significant influence over the behaviour of the turbulence quantities. When using only the $k - \omega$ SST model, transition starts at very low Reynolds numbers and this effect is hidden. This decay means that k set at the inlet will be lower when reaching the leading edge of the airfoil. The decrease is more pronounced in both k and ω then for $\frac{\mu_t}{\mu}$. There are some options to mitigate this effect.

The easiest option is to set a higher $\frac{\mu_t}{\mu}$ in order to minimize the decay of the other quantities. However, care must be taken when doing this, since too high values of μ_t compromise the laminar part of the solution. Other option is referred as frozen decay, in which one can deactivate the destruction terms in the turbulence model equations. One other option is the introduction of weak source terms that become negligible in the boundary layer. Of course, every option comes with drawbacks and is up to the user to decide.

For this project, a conscious choice to neglect this effect, was made. Meaning, none of the above options were chosen, with the author setting the values at the inlet and not trying to mitigate the effect of turbulence decay.

Chapter 4

Methodology

The following section outlines the NACA 0012 airfoil mesh and flow calculations procedure. Both meshing and solving were performed with the CFD software *STAR-CCM+*.

4.1 Initial Methodology

The initial approach of the present work, to study dynamic stall, was completely different to the approach that ended up coming to fruition. The first plan was to study dynamic stall using the wake of a bluff body, a cylinder. The vortex shedding resultant from the flow past a cylinder is well studied and the frequency of these vortices is also well documented. These frequencies can be calculated (and controlled) from the Strouhal number, St defined as:

$$St = \frac{fd}{U_\infty} \tag{4.1}$$

with f being the vortex shedding frequency, d the reference length and U_∞ the flow velocity.

The plan at the beginning was to simulate the flow past a cylinder and varying both d and U_∞ (and with this, the Reynolds number), calculate the St from the software and compare it with experimental data on St vs Re. Having the St value, one could then compare it with some dynamic stall experiments (the shedding frequency would need to be matched with the reduced frequency of the chosen experimental study). In fact, several simulations were performed by the author to study the flow past a cylinder and several more with an airfoil at some distance past the cylinder.

There were several reasons as to why the method was abandoned. Firstly, it was very difficult to know the exact AoA variation experienced by the airfoil. Due to the “wavy-behaviour” of the so called Von-Kárman street, determining the AoA by inspecting the streamlines was very hard. Too close to the airfoil the streamlines are affected by its presence and too far downstream, the measured variation would be much higher than the one felt by the airfoil. Because of this, the sole measurement of the AoA would be affected by non-negligible errors. Furthermore, the streamlines close to the centreline of the Von-Kárman street have an abrupt change in direction, reason why the airfoil had to be positioned with some y displacement, relative to the centreline. This new, vertically changed, position caused several problems also. If the airfoil is too close to the centreline, the AoA variation experienced is still greater than wanted and if it is too far away the flow is not perturbed and there is no variation. Choosing an appropriate position whose AoA variation was in accordance to experimental studies revealed to be very difficult.

Given the reason aforementioned, no relevant results were obtained regarding the dynamic stall study using the cylinder's wake. After two months of simulations, the idea was substituted by a more practical and feasible methodology, presented below.

4.2 CFD of NACA 0012

4.1.1 Geometry

A computer-aided design (CAD) of a NACA 0012 was used in the CAD software *SOLIDWORKS*. A scaling of the model can be easily done, so any chord length can be chosen. After verifying the model, it was then imported to the meshing software, *STAR-CCM+.*

The 2D geometry process is quite easy and straight-forward, one of the reasons for using the software. The imported CAD model was put in the center of the sketch. The second phase is to choose how the user wants the computational domain to be.

An iterative procedure was adopted to determine how large the domain had to be. Both Figure 16 and 17 present the dimensions of the domain of static and unsteady simulations, respectively.

4.1.2 Mesh

An unstructured mesh allows for a rapid local mesh refinement exercise for RANS flow calculations. The main advantages of this mesh type are that it provides a rapid generation of a mesh for complex geometries and also allows the generation of refined regions, which is important to capture the unsteady flow phenomena.

Before simulating the dynamic stall, three different meshes were created (coarse, medium and fine mesh). These meshes, were then used to simulate the steady stall at diverse AoA and the obtained results compared with the experimental results from [51]. The objective was to reach a balance between the available computational power and the accuracy of the results, giving the author sensitivity to how refined the mesh had to be to study the unsteady phenomena. The control of cells size was possible due to a parameter the software has, designated cells' base size. This parameter regulates the size of the cells in the mesh. The refinements were done by changing the relative size of the cells in that region. This is very useful as one can easily control the mesh size by simply changing the cells base size and all the refined regions will also change, maintaining its proportion. The only mesh that was set in terms of absolute size and not in relative size, was the prism layer mesh.

In this work, the regions of interest were the upper surface, LE (due to flow separation there) and the wake. For this reason, the approach was to generate four increasingly denser regions, progressively closer to the airfoil: the first one, composed of cells with an approximate dimension of 65% of the base size and extended for 12 meters (equivalent to $20c$) in all directions, starting from the LE; the second, extended 6 meters starting at the LE in all directions, had cells with 30% of the base size; the third refinement zone, had cells with approximate 10% of the base size and extended 4.5 meters in all directions. Finally, the densest region in the computational domain, composed of cells with 0.95% of

the base size, extended for 1.5 meters in all directions. The cells growth factor was set to 1.2 in all zones, allowing a smooth transition between refinement zones.

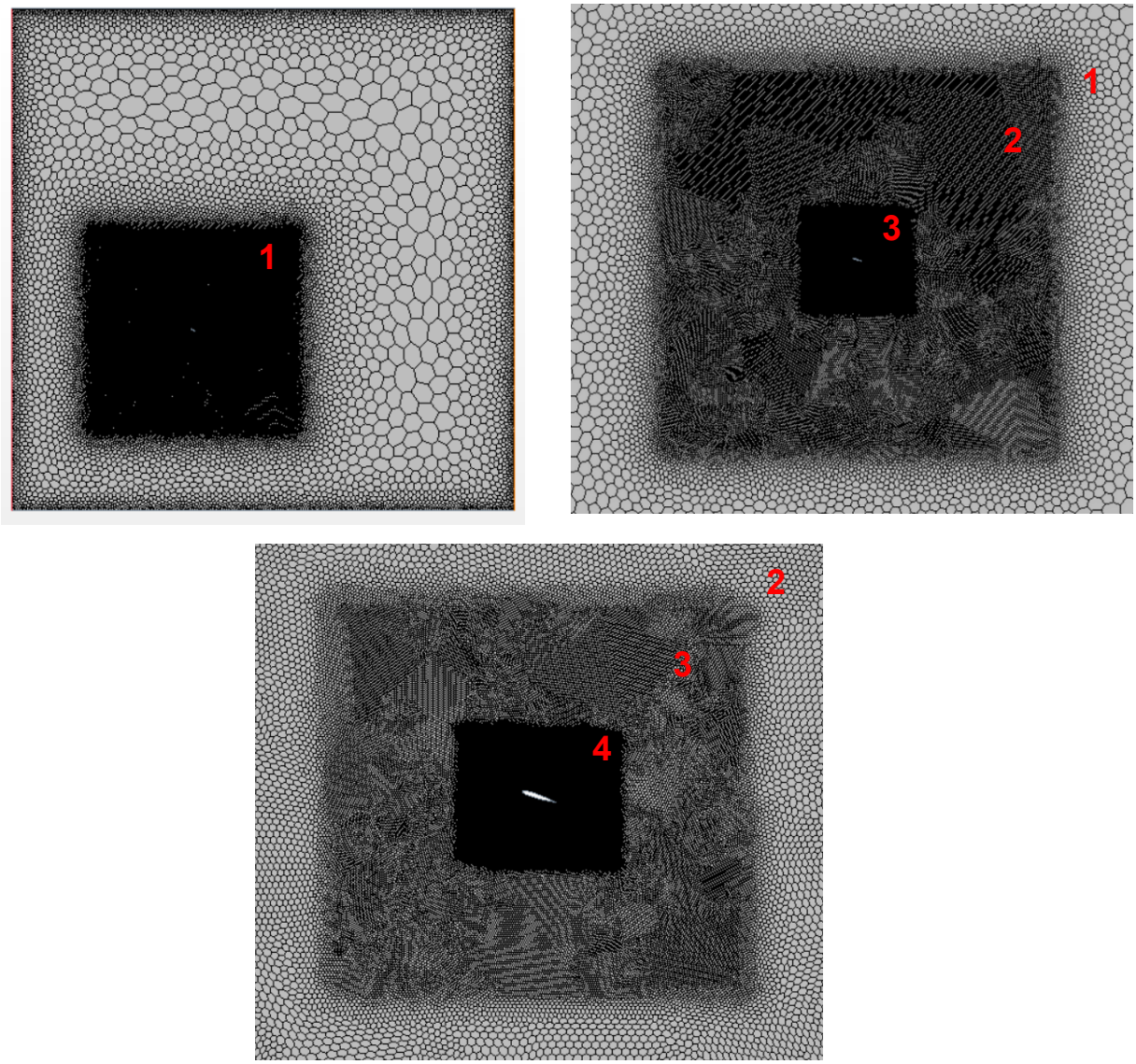

Figure 11: Mesh structure and refinement zones. 1- First refined zone 2- Second refined zone 3- Third refined zone 4- Most refined zone around the airfoil

Table 3: Three tested meshes' density (Million Cells)

Parameter	Coarse	Medium	Fine
Density (10^6 cells)	1.5	3.5	6.0

One very crucial region is the boundary layer and in order to model it, prism layers were used. Three important parameters had to be defined: the near wall layer thickness, the total prism layer thickness and the number of prism layers. Figure 12 represents the normalized velocity profile in a turbulent boundary layer and its regions.

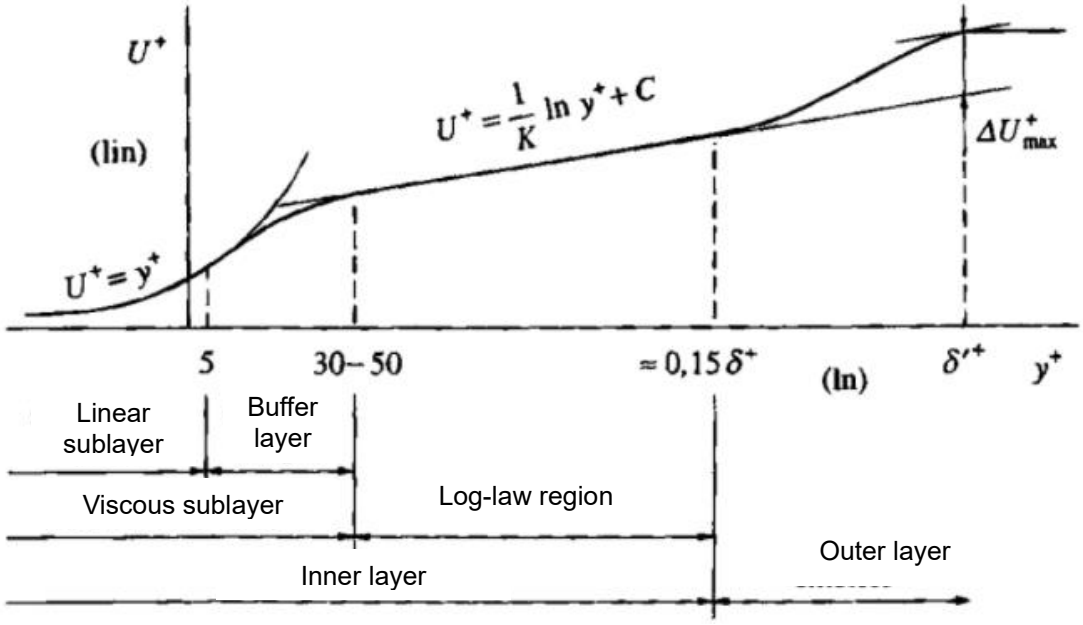

Figure 12: Normalized velocity profile in a turbulent boundary layer (Adapted from [2])

In order to proper solve the linear sublayer region, which is the region closest to the wall, y^+ (dimensionless wall distance) must be smaller than 1. Regarding the near wall prism layer thickness (or height), it corresponds to Δy_1 in Equation 4.2, where u_τ is the friction velocity. The first cell height is obtained with the following expression:

$$y^+ = \frac{\rho u_\tau \Delta y_1}{\mu} \tag{4.2}$$

To obtain u_τ, the skin friction coefficient C_f has to be computed, followed by the wall shear stress τ_w and finally calculating the friction velocity. An important assumption was made to obtain these calculations. The formulas presented below, are for a turbulent boundary layer in a flat plate. The values obtained are good first estimations to introduce in the software and then, iteratively, check the y^+ obtained.

$$C_f = 0.058 Re_c^{-0.2} \tag{4.3}$$

$$\tau_w = \frac{1}{2} C_f \rho U_\infty^2 \tag{4.4}$$

$$u_\tau = \sqrt{\frac{\tau_w}{\rho}} \tag{4.5}$$

The decision to model the boundary layer without wall functions was based on two factors. Preliminary simulations concluded that when wall function were not used, the correlation between the computed aerodynamic coefficients and the experimental results were better. The second reason is that

using wall functions, a fully turbulent flow would be assumed. Despite this might be the case for about 95% of the chord, not even accounting the increase in AoA leads the transition point even closer to the LE, the laminar bubble is rather important when studying stall for a NACA 0012 profile. Regarding the possible wall treatments in *Star-CCM+*, the software has three options:

Low y^+: The linear sublayer is calculated without wall functions. Shear stress at the wall, τ_w, is calculated by its definition (this was the chosen option):

$$\tau_w = \mu \left.\frac{\partial U}{\partial y}\right|_{y=0} \tag{4.6}$$

High y^+: This wall treatment implies the usage of wall functions, namely that the cells nearest to the wall are in the log-law region. The viscous sublayer is not resolved and the prism layer mesh does not need to be too refined.

All y^+: Hybrid model which tries to conciliate both previously mentioned methods and is formulated by solution for meshes whose cells close to the wall do not discretize independently the different turbulent boundary layer regions.

The total prism layer thickness controls the overall thickness of all the prism layers. To estimate the boundary layer thickness was used the Von Kárman equation, which is deduced for fully turbulent flows, so it can be only used as an approach to estimate the required prism layer thickness:

$$\delta = \frac{0.37c}{Re^{0.2}} \tag{4.7}$$

The total prism layer thickness ended up being set to a slightly larger value than the obtained from Equation 4.7. This equation only gives us an estimation and so it was used as a first estimation of the boundary layer thickness. It was, then, iteratively changed until the desired y^+ was obtained.

The total number of prism layers (N) is the parameter controlling the number of layers present in the mesh closer to the profile. As this number increases, the refinement of the mesh close to wall is greater, consequently discretization errors decrease. To model the boundary layer without wall functions, N has to be quite larger comparative to the number of prism layers to model it with wall functions. It must be large enough, in order to have enough layers in each zone to properly discretize the boundary layer zones independently. This number, however, leads to greater computational effort, which was the main constraint of this work. A balance had to be done and a great number of tests were done.

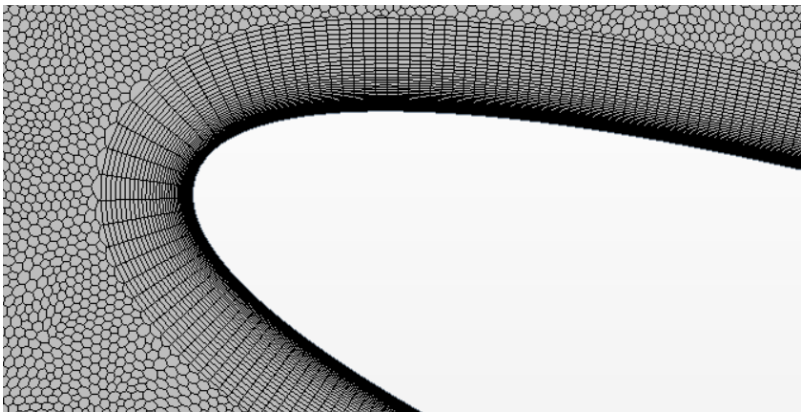

Figure 13: Prism layer mesh used around the LE of the airfoil

The final value was chosen to be $N = 70$, with hyperbolic tangent as stretching function, in order to have a smooth transition between the layers further from the wall. Table 4 presents the calculations performed for the steady simulations (for the unsteady case, the Reynolds number was different. However, the process and calculations are similar).

Table 4: Values used in the first iteration, for static simulations

Re	δ	C_f	τ_w	u_τ	Δ_{y1}	N
2.7×10^6	0.0115	0.0030	8.2829	2.622	1.817×10^{-6}	70

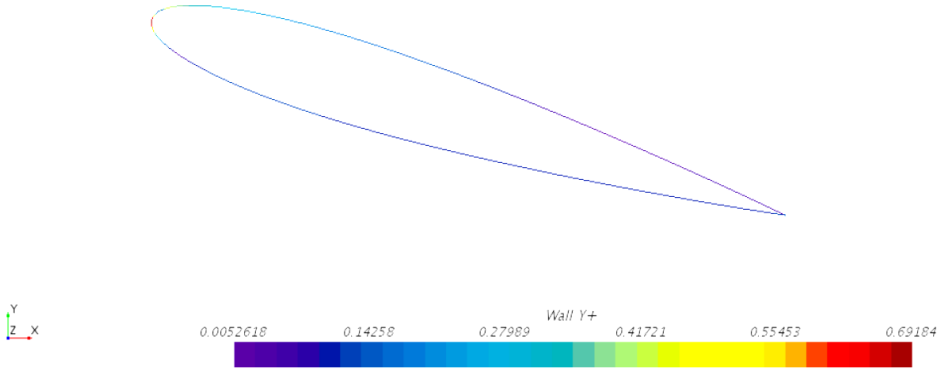

Figure 14: y^+ values for the steady simulation with $\alpha = 16º$, stall angle

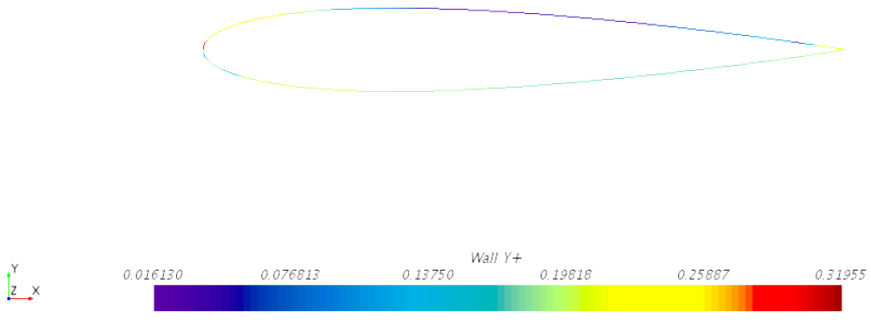

Figure 15: y^+ values for an unsteady simulation performed

4.1.3 Numerical Solving

The chosen commercial software, as previously said, was *Star-CCM+* for the numerical calculation performed. It has many capabilities essential for the present work, namely the modelling of incompressible, inviscid flows, both laminar and turbulent, with transition models available, steady and unsteady (transient) fluid flows.

As already mentioned, calculations were performed with the two-equation model $k-\omega$ SST model, coupled with $\gamma - Re_\theta$ transition model. The solver can be chosen between pressure-based and density-based solver. Both numerical methods use the finite-volume method approach, with the pressure-based solving a pressure equation, formulated from the continuity and momentum equations, so that the velocity field, corrected by the pressure, satisfies the continuity equation. The density-based solver solves the governing equations of continuity, momentum, energy and species transport simultaneously. The decision to use the pressure-based solver was supported by the fact that this solver is mostly used for incompressible flows, which is the case of the present work (it has to be said that in recent versions, both pressure-based and density-based solvers can be used outside their original intent).

The governing equations might be linearized in an explicit or implicit manner. The implicit formulation was chosen due to being faster to achieve convergence, although at the cost of higher memory requirements. Implicit formulation means the unknown value in each cell is computed from both existing and unknown values of the neighbouring cells.

In the spatial discretization, the gradient chosen was the Hybrid Gauss-LSQ (Least Squares) which according to *Star-CCM+* user manual, comes as an improvement of the Green-Gauss. It works as a blending between the Hybrid Least Squares gradient reconstruction and the Green-Gauss. The spatial discretization was also chosen as second-order. Hence second-order upwind scheme was applied. As a limiter, the software, by default, chooses the Venkatakrishnan limiter, which was not altered for any simulation.

For the unsteady simulation, *Implicit Unsteady* model was the option chosen. The CFL number, in theory, can be even higher than 100, however, non-linearities in the governing equations can limit stability, depending on the problem's complexity. So, simulations began with a CFL of 1, and it was increased, gradually, to 5 and even 10. This was an advantage since larger time steps would lead to a faster convergence.

For steady simulations, *Steady* model was chosen.

4.1.3 Boundary conditions

4.1.3.1 Steady Simulations

For the static simulations, the computational domain and boundary conditions are present in Figure 16.

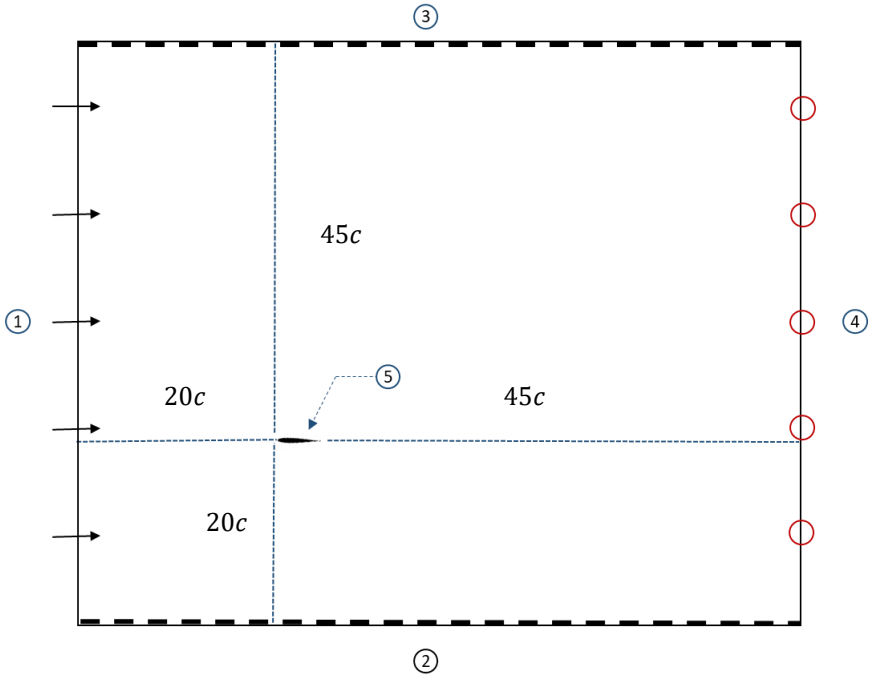

Figure 16: Computational domain for static simulations and boundary conditions (not at scale)
1 – *Inlet*; 2 – *Bottom*; 3 – *Top*; 4 – *Outlet*; 5 – *Airfoil*.
Arrows: Velocity inlet condition; Black dashed lines: Slip wall condition; Red circles: Pressure outlet

It is normally advised to have a domain's length of at least ten times the characteristic length of the body being studied and then one has to take into account the distance to both top and bottom walls and decide to include, or not, the effect of wall blockage. For this study, the domain's size was the same for the unsteady and steady simulations, reason why the utilized domain for steady simulations is much larger than the typical. Furthermore, the airfoil was kept in the same position as in the unsteady simulations, leading to the airfoil not being at the same distance from *Top* and *Bottom*, as usually is.

The computational domain defines 5 boundaries, to which three boundary conditions were applied, as the legend of Figure 16 states. The boundary conditions were:

1. At the *Inlet* boundary, velocity inlet type condition was applied. Besides velocity, turbulence intensity and turbulent viscosity ratio had to be defined. Not all documents about experimental results for a pitching NACA 0012 had information about the turbulence intensity. The value of 1% was set for all simulations, resulting in $k = 1.5 \times 10^{-4} U_{\infty}^{2}$. Since $k - \omega$ SST was the turbulence model used, ω remain to be set. To set the value of ω is not particularly easy. The author considered the advice of Professor Luis Eça, Senior Lecturer of Aerodynamics course at IST, and instead set $\frac{\mu_t}{\mu}$ which is easier and attainable with:

$$\frac{\mu_t}{\mu} = Re \times 10^{-8} \tag{4.8}$$

2. Both *Top* and *Bottom* were defined as walls with slip type condition.

3. At the *Outlet* boundary, pressure outlet condition was applied. It is a typical condition to be applied at the boundaries where the flow exits the domains.

4. The surface of the airfoil is, of course, treated as a solid wall: no-slip and impermeability conditions were used.

To study the steady stall the AoA of the airfoil changed for each simulation. This, of course, took some valuable time, given that every AoA implied a new meshing procedure. Other alternative, a better one, would have been to adopt the procedure of unsteady simulations, which in this case would mean the airfoil at null AoA with the fluid reaching the airfoil with the desired AoA. Also, this alternative had a faster implementation.

4.1.3.2 Unsteady Simulations

In Figure 17 it is possible to see the domain and boundary conditions used for the unsteady case. The large size of the domain is particularly important for the unsteady simulations since for those simulations the airfoil was fixed at null AoA and it was the flow behaving according to Equation 2.3, simulating the pitching motion. Shortly, it will be seen how to implement this method in the software.

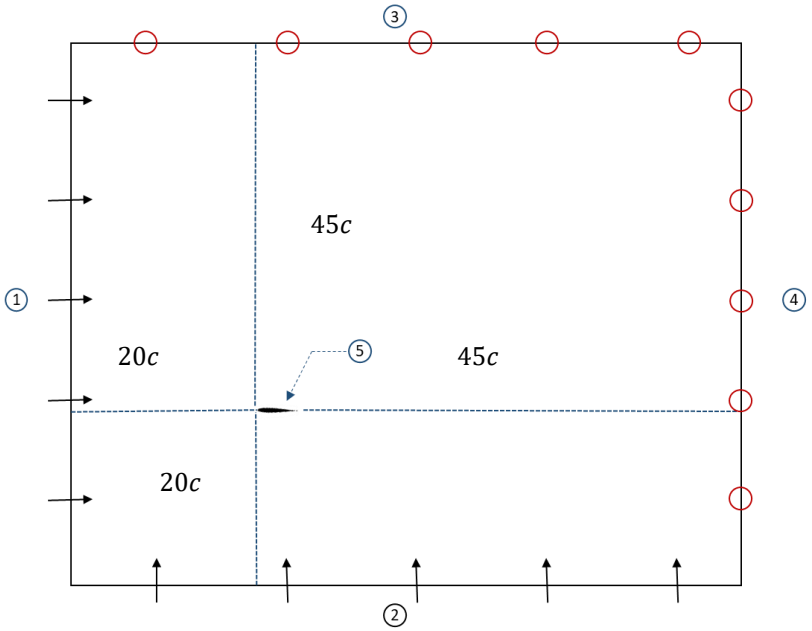

Figure 17: Computational domain for unsteady simulations and boundary conditions (not at scale)
1 – *Inlet*; 2 – *Bottom*; 3 – *Top*; 4 – *Outlet*; 5 – *Airfoil*.
Arrows: Velocity inlet condition; Red circles: Pressure outlet

The computational domain defines 5 boundaries, to which three boundary conditions were applied, as the legend of Figure 17 states. The boundary conditions were:

1. At the boundaries called *Inlet* and *Bottom*, velocity inlet type condition was applied. Similar to the steady simulations, k and $\frac{\mu_\tau}{\mu}$ were set.

2. At the boundaries called *Top* and *Outlet*, pressure outlet type condition was applied. However, for the present work a large domain had to be used for these conditions to be met.
3. In the airfoil, no-slip boundary condition was set.

In order to simulate the pitching movement, with the fluid obeying the required motion equation instead of the airfoil, various *Field Functions* were created. The direction of fluid entering the domain was changed from *Boundary-Normal* to *Composite,* allowing the user to define the flow in each direction. Two different *Field Functions* were created: x_{dir} and y_{dir} , being defined, respectively as:

$$x_{dir} = \cos\lfloor\bar{\alpha} + \tilde{\alpha}\sin(wt)\rfloor \tag{4.9}$$

$$y_{dir} = sin[\bar{\alpha} + \tilde{\alpha}sin(wt)] \tag{4.10}$$

This means the fluid enters the domain with velocity magnitude U and its two components being:

$$U_x = U\cos\lfloor\bar{\alpha} + \tilde{\alpha}\sin(wt)\rfloor \tag{4.11}$$

$$U_y = U\sin\lfloor\bar{\alpha} + \tilde{\alpha}\sin(wt)\rfloor \tag{4.12}$$

When dealing with time-dependent motions of bodies, the coordinate system selection is very important. The coordinate system fixed in the airfoil is stationary (inertial), however, the fluid is "pitching", meaning its reference frame is non-inertial, reason why an acceleration field must be introduced. Acceleration is obviously obtained from deriving U_x and U_y.

$$\frac{dU_x}{dt} = -U_\infty\tilde{\alpha}w\cos(wt)\sin\lfloor\bar{\alpha} + \tilde{\alpha}\sin(wt)\rfloor \tag{4.13}$$

$$\frac{dU_y}{dt} = U_\infty\tilde{\alpha}w\cos(\mathrm{wt})\cos\lfloor\bar{\alpha} + \tilde{\alpha}\sin(wt)\rfloor \tag{4.14}$$

In terms of the software this is attainable by adding a *Momentum Source Option*, defining it as a *Composite* and creating two new *Field Functions*, which in this case were called: $Mom.Source_x$ and $Mom.Source_y$.These momentum source functions have Force/Volume unit, meaning Equation 4.13 and 4.14 above are inserted as:

$$Mom.Source_x = -\rho U_\infty\tilde{\alpha}w\cos(wt)\sin\lfloor\bar{\alpha} + \tilde{\alpha}\sin(wt)\rfloor \tag{4.15}$$

$$Mom.Source_y = \rho U_\infty\tilde{\alpha}w\cos(\mathrm{wt})\cos\lfloor\bar{\alpha} + \tilde{\alpha}\sin(wt)\rfloor \tag{4.16}$$

This method, however, does have some limitations. First of all, incompressible flow simulations do not allow for very high Re to be tested correctly, since at the LE of the airfoil transonic or even supersonic flow might occur. Secondly, and directly related with having the airfoil steady and having the flow vary the angle of incidence, the pitching motions possible to be tested are limited. Only pitching motions having $\bar{\alpha} > \tilde{\alpha}$ could be tested with this method, meaning negative AoA could not be tested.

4.1.4 Data Acquisition

This subsection outlines, in a brief manner, the method for obtaining the desired data, presented in Section 5**.** This covers both static and unsteady simulations results.

In terms of aerodynamic coefficients, these can be obtained from the software. Both C_l and C_d are obtained from the software section *Reports*. The user must set a reference velocity, the pressure (gauge), the reference area, reference density, the direction and the force option (pressure and/or shear stress). The reference velocity is the freestream velocity and reference density is the density of the gas. The reference area, for a 2D simulation is equal to the chord length, c, times a unitary span.
For C_m two other parameters are needed. The location of the axis around which C_m will be calculated and a reference radius, which is a reference length, in the present the case, the chord length. Any other coefficient, like C_p or C_f is obtained from an *XY Plot*, with only having to introduce the reference density and reference velocity values for the correspondent coefficient, in the separator *Field Functions.*

Also, the software does not allow any data-processing or manipulation. The user has then the possibility to export all this data and treat it in a suitable software.

4.1.5 Numerical Error

Numerical error associated to a numerical calculation is constituted by three components: round-off error, iterative error and discretization error. Round-off error is the computer's limitation and precision limits on their ability to represent numbers. This error grows with the number of cells. Iterative error originates from the non-linearity of equation to be solved, like the RANS equations and can be reduced. Lastly, discretization error comes from the approximations made to transform the partial differential equations of the continuum formulation into a system of algebraic equations [52]. Unlike the other two errors, discretization error reduces with the mesh refinement. As stated by Eça [52] the iterative error should be two to three orders of magnitude smaller than the discretization error and one can assume (as it will be in the present work) that the contribution of the round-off error is negligible compared to the discretization error. The estimation of discretization error can be done with a systematic mesh refinement.

For the estimation of the discretization error, the method proposed by Eça [52] was used. This model affirms that U_{num}, numerical uncertainty, is given by

$$U_{num} = F_S|\delta_{RE}| \tag{4.17}$$

where F_S is a safety factor with value 1.25 and $|\delta_{RE}|$ the numerical error estimation defined as:

$$\delta_{RE} = \Phi_i - \Phi_0 \tag{4.18}$$

Φ_i stands for any integral or other functional of a local flow quantity, Φ_0 is the estimate of the exact solution. In order to determine Φ_0 , a methodology based on the grid refinement ratio was used. Different meshes were related with each other according to:

$$r_i = \sqrt{\frac{h_1}{h_i}} \tag{4.19}$$

where r_i is the grid refinement ratio of mesh i, h_i the number of cells of mesh i and h_1 the number of cells of the more refined mesh.

After defining the grid refinement ratio, a linear interpolation of the various numerical results was done, considering the numerical results obtained for each mesh and the respective grid refinement ratio.

This interpolation results in a line whose y for $x = 0$ corresponds to a grid refinement ratio of zero, i.e., a mesh with an infinite number of cells, where the discretization error is assumed to be zero and this y value would then be Φ_0 . In order to have a good estimate of the exact solutions it was necessary to consider three meshes (as the number of used meshes increases, the precision of the estimation grows).

The numerical uncertainty associated to each mesh can then be calculated and help define an interval of values containing the numerical solution, with 95% coverage.

$$\Phi_i - U \leq \Phi_{exact} \leq \Phi_i + U \tag{4.20}$$

In order to compare the obtained numerical data with the experimental data, the relative error between both is calculated, with this error given as:

$$e_{rel} = \frac{|\Phi_0 - \Phi_{exp}|}{\Phi_{exp}} \tag{4.21}$$

where Φ_{exp} is the experimental value of the analysed parameter.

Chapter 5

Results

In this chapter the mesh sensitivity analysis is performed and the results obtained from the CFD simulations are analysed and compared. The static stall on NACA 0012 was simulated with $k-\omega$ SST + $\gamma - Re_\theta$ and C_f and C_p for three different AoA are presented: $14º$ (pre-stall) , $16º$ (stall) and $18º$ (post-stall). Furthermore, the velocity vector field is also presented for each one of those AoA. Afterwards light stall results are presented and deep stall results. For deep stall analysis, vorticity and velocity fields during the cycle are shown and $-C_p$ plot of some AoA of interest.

An analysis regarding the influence of κ and Re on dynamic stall is also performed.

5.1 Mesh Analysis

A mesh sensitivity analysis was performed, for three solutions at different AoA obtained from the steady flow calculations, in order to evaluate the most suitable mesh with which the simulation could be performed. The goal was always to achieve good results in terms of accuracy and computational time. In order to understand the influence of such meshes, lift, drag and momentum coefficients were compared for each one of them. Then these results were compared to the experimental results of [51]. All studies were performed for the same conditions, as seen in Table 5:

Table 5: Parameters of experimental studies [51] and computational static simulations

	$\boldsymbol{c(m)}$	$\boldsymbol{U_\infty(m/s)}$	$\boldsymbol{Re(10^6)}$	$\boldsymbol{\rho(kg/m^3)}$	$\boldsymbol{\mu(Pa\ s\ \times 10^5)}$
Experimental	0.601	68,0	2.66	–	–
Computational	**0.600**	**67.7**	**2.70**	**1.2047**	**1.815**

Table 6: Normalized residuals for convergence criteria

Continuity	***Momentum x***	***Momentum y***
10^{-5}	10^{-5}	10^{-5}

The results of C_l and their respective uncertainty are presented in Figure 18 and Table 7, respectively. The results are shown from the null AoA until AoA of $18°$, which is after stall happens, meaning there are nine different AoA presented in this section. This allows for an analysis of low AoA, pre-stall AoA, stall AoA and post-stall AoA and observe how each mesh did on calculating the aerodynamic coefficients.

As expected, for low AoA, both experimental and computational results agree very well with each other and do not differ much from the results obtained for an ideal fluid. In fact, up until $\alpha = 10°$, C_l remains approximately linear. At higher AoA viscous effects become too important and C_l values start to differ from those of an ideal fluid. All three meshes, from $\alpha = 0°$ to $\alpha = 12°$, predict very similar values for C_l. This is also in accordance to the expectations, since a not so refined mesh should be able to compute good results for the C_l of a symmetric airfoil at low AoA.

For $\alpha = 14°$, which is an AoA close to the stall AoA, the coarse mesh predicts a higher value than the other two meshes. In fact, other than $\alpha = 16°$, the coarse mesh predicted higher values than the more refined mesh. Both medium and fine mesh agree well with each other and with the experiment. The stall AoA, $\alpha = 16°$, was the first reason why the coarse mesh was discarded. Firstly, the coarse mesh completely fails to capture the lift increase from $\alpha = 14°$ to $\alpha = 16°$. Secondly, the calculated C_l with this mesh diverges from the experimental values and the other two meshes values. Thirdly, if one looks at the post-stall AoA, $\alpha = 18°$ and observe the general trend of the C_l for the coarse mesh, one might assume to be in the presence of TE stall, given the smooth decrease in the lift coefficient. Furthermore, the coarse mesh also completely fails to compute the post-stall flow dynamics, which coupled with its high uncertainty, led to the author discarding this mesh from potential mesh to be used on dynamic simulations (although its computational time is much less than the other two refined meshes).

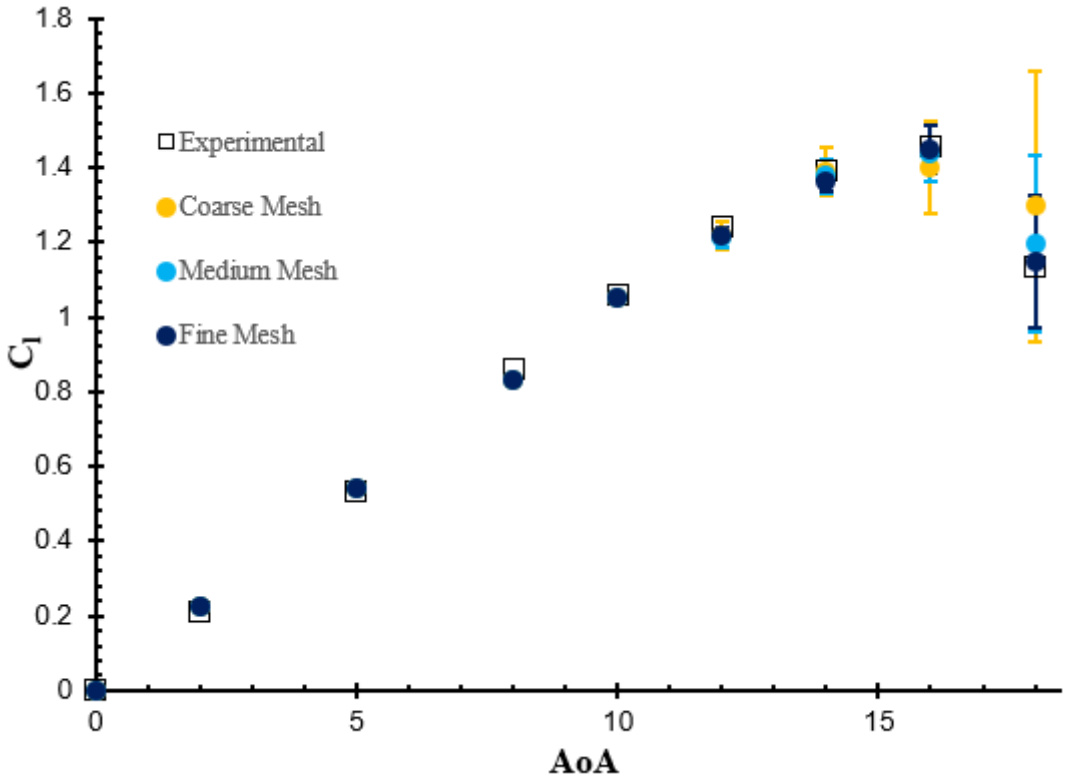

Figure 18: C_l for the three tested meshes, affected by their respective uncertainty. Experimental results from [51]

Both medium and fine meshes predicted well the stall angle, with its uncertainties not being as high as the author expected, *a priori*. The post-stall C_l is where these two meshes predicted different values.

The experimental results of Ladson [51] pointed to a post-stall $C_l = 1.134$ whereas the medium mesh and fine mesh to $C_l = 1.196$ and $C_l = 1.148$, respectively. The fine mesh did clearly predict a closer C_l to the experimental one. The uncertainty, however, is quite high for both cases. The relative error for this AoA was $e_{rel} = 11.3\%$.

Table 7: C_l results obtained with the three tested meshes and their respective uncertainties. Experimental data from [51]

AoA	Experimental	Coarse	Medium	Fine
0	–	–	–	–
2	0.214	0.225	0.225	0.225
5	0.534	0.544	0.544	0.544
8	0.859	0.832 ± 0.003	0.830 ± 0.0005	0.831 ± 0.0018
10	1.059	1.053 ± 0.008	1.050 ± 0.00425	1.050 ± 0.0043
12	1.244	1.220 ± 0.0379	1.212 ± 0.0279	1.205 ± 0.0191
14	1.394	1.390 ± 0.063	1.377 ± 0.0478	1.365 ± 0.0318
16	1.456	1.399 ± 0.125	1.440 ± 0.0754	1.448 ± 0.0654
18	**1.134**	$\mathbf{1.296 \pm 0.3625}$	$\mathbf{1.196 \pm 0.2375}$	$\mathbf{1.148 \pm 0.1775}$

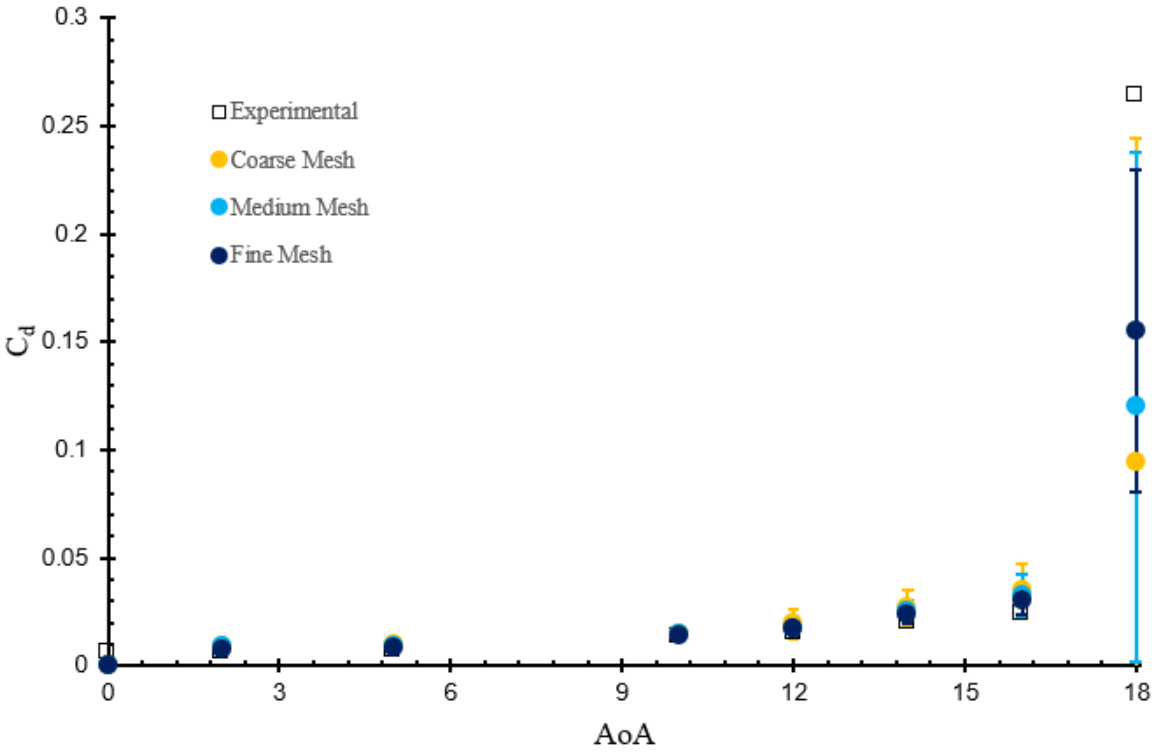

Figure 19: C_d values for the three tested meshes, affected by their respective uncertainties. Experimental results taken from [51]

Figure 19 presents the C_d for the studied values of AoA. There is great accordance between all meshes and experimental values until $\alpha = 12°$, similarly to what was verified with C_l. At $\alpha = 14°$ the coarse mesh slightly over predicts the drag coefficient, $C_d = 0.027$, in comparison to experimental value of $C_d = 0.0204$. For $\alpha = 16°$, the three meshes clearly over predict the drag, with the fine mesh predicting better than the other two meshes, naturally.

For $\alpha = 18°$ neither mesh was able to capture a drag increase, resultant from stall, as high as the experimental results. Nonetheless, all of the studied meshes predicted a great increase in drag for $\alpha = 18°$.

Table 8: C_d results for the three tested meshes and their respective uncertainties. Experimental data from [51].

AoA	Experimental	Coarse	Medium	Fine
0	0.00607	–	–	–
2	0.00612	0.009 ± 0.0035	0.0088 ± 0.00325	0.0075 ± 0.0016
5	0.0071	0.0097 ± 0.0034	0.0091 ± 0.0026	0.0083 ± 0.0016
10	0.0132	0.015 ± 0.002	0.0147 ± 0.0016	0.0142 ± 0.001
12	0.01517	0.0196 ± 0.0069	0.0174 ± 0.0041	0.017 ± 0.0036
14	0.0204	0.027 ± 0.0078	0.025 ± 0.0053	0.024 ± 0.004
16	0.0242	0.035 ± 0.0123	0.033 ± 0.0098	0.030 ± 0.006
18	**0.2642**	$\mathbf{0.094 \pm 0.151}$	$\mathbf{0.120 \pm 0.1181}$	$\mathbf{0.155 \pm 0.074}$

Besides C_l and C_d, a closer look at C_m is also important. The following results were obtained for the C_m about $0.25c$. As already expected from the analysis of C_l and C_d, the coarse mesh predicted very erroneous results for the C_m, meaning its computation of pressure and flow dynamics around the airfoil were not being rightly computed. Those results were considered as noise and discarded, leading to only two meshes having acceptable results of C_m. The major problem arising from this is that for C_m not enough mesh values are available to the validation procedure. Hence, the results present in Figure 20 and Table 9 are only for the Medium and Fine meshes and there are no values for their respective uncertainties.

Both medium and fine meshes, until $\alpha = 14°$ predict very well the pitching moment of the airfoil. At $\alpha = 14°$ both meshes overpredicted C_m and had a larger difference relative to the experimental value, than for the stall angle, $\alpha = 16°$. The main focus when evaluating C_m predicted from both meshes was the post-stall state of the airfoil. For the unsteady simulations, it was important to have a mesh that could predict, as accurate as possible, the pitching moment stall. Both meshes did predict the post-stall pitching moment reduction, with the medium mesh predicting $C_m = -0.089$ and the fine mesh $C_m = -0.081$. The medium mesh, relatively to the fine mesh, overpredicted the pitching moment for this AoA.

The choice between utilising a fine or medium mesh was not taken lightly. The fine mesh did better predicting the pitching moment for the post-stall conditions and also the drag increase for this

AoA. When testing the fine mesh in an unsteady simulation, the computational time was unfeasible. For this reason, the medium mesh was the chosen for the unsteady simulations.

Ideally, the fine mesh would have been the mesh used in all unsteady simulations, for better accuracy. Nonetheless, as the static results proved, the medium mesh did predict well the aerodynamic coefficients in all stages (exception for the C_d in post-stall conditions).

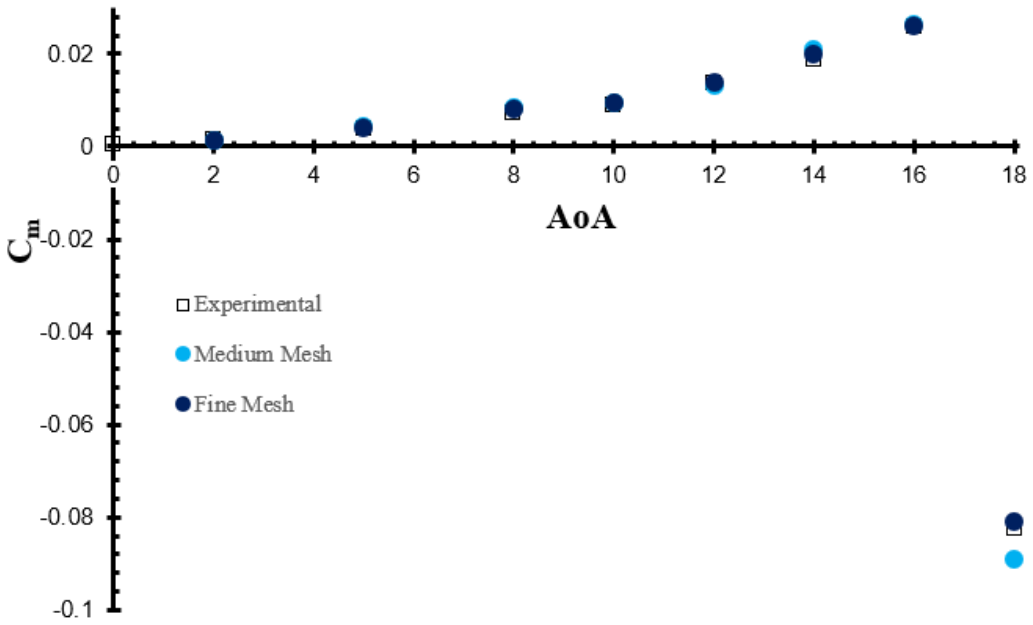

Figure 20: C_m for the medium and fine meshes. Experimental results taken from [51]

Table 9 - C_m about $0.25c$ for the medium and fine meshes. Experimental results taken from [51]

AoA	Experimental	Medium	Fine
0	0.0004	–	–
2	0.0016	0.00129	0.0015
5	0.004	0.0045	0.0042
8	0.0074	0.0083	0.0081
10	0.0091	0.00947	0.0094
12	0.0138	0.0133	0.0138
14	0.0189	0.0211	0.0199
16	0.02576	0.0264	0.0260
18	**−0.0823**	**−0.089**	**−0.081**

Evaluating the mesh based solely on its numerical error, uncertainty and computational time, may not be enough. Ergo, the flow physics was also analysed in order to better understand if the medium mesh produces physically accurate solutions.

Figure 22 presents $\alpha = 16°$, whose C_l and C_d are slightly under-predicted and over-predicted, respectively. The velocity field across the upper surface of the airfoil, indicates that the flow separation region is over predicted, meaning the area of separated flow in the computational simulations is larger than the real separated area from the experimental case. This would explain the under prediction of the lift coefficient and at the same time the over prediction of the drag coefficient, since it increases (largely) when separation is present.

For $\alpha = 18°$, the post-stall situation, the situation is the opposite. C_l from simulations is larger than the experimental and C_d is much smaller than the expected. Comparing the velocity fields for both AoA, there is a clear increase in the separation area for the post-stall angle, as one would expect. However, this area increase might not be as large as the increase verified in the experimental studies, reason why there is such a large difference in drag.

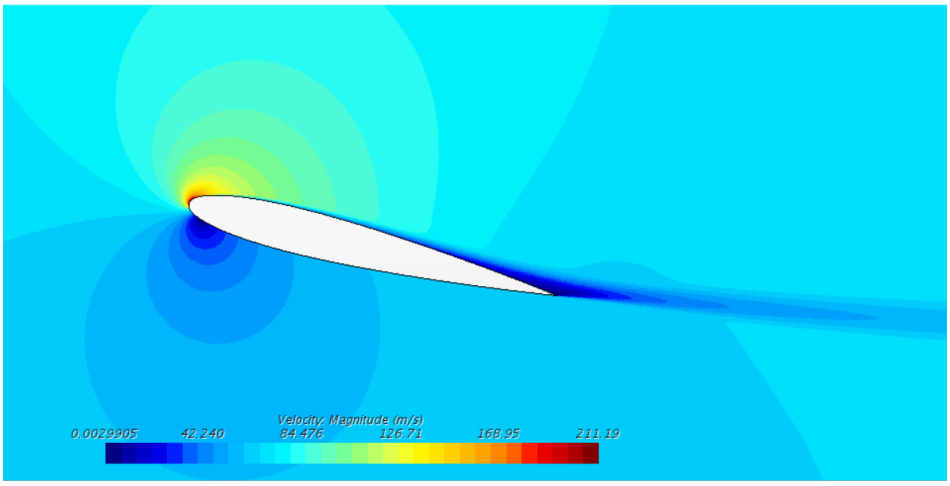

Figure 21: Velocity field for $\alpha = 14°$

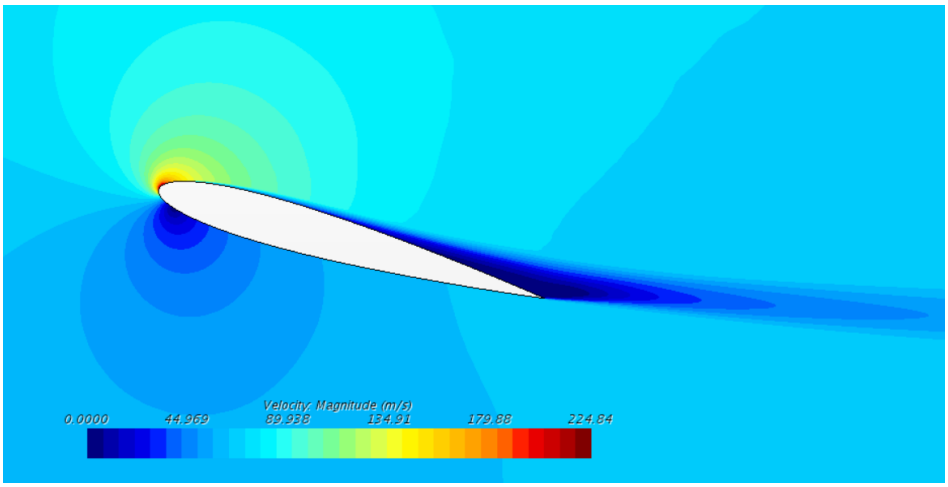

Figure 22: Velocity field for $\alpha = 16°$

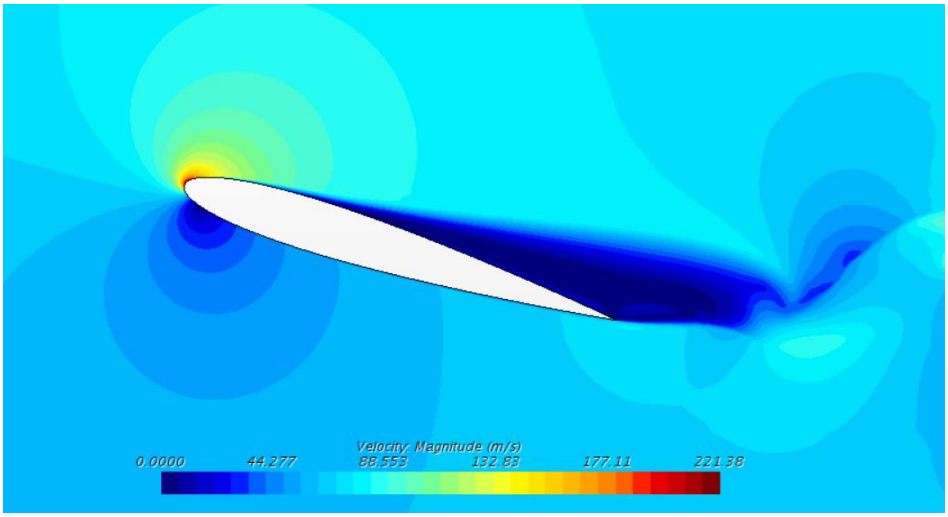

Figure 23: Velocity field for $\alpha = 18°$

5.2 Static stall NACA 0012 with Medium Mesh

This section presents the results obtained from the steady simulations using a medium refined mesh. The pressure coefficient, C_p and the skin friction coefficient, C_f for three different AoA, at different stall stages, are presented.

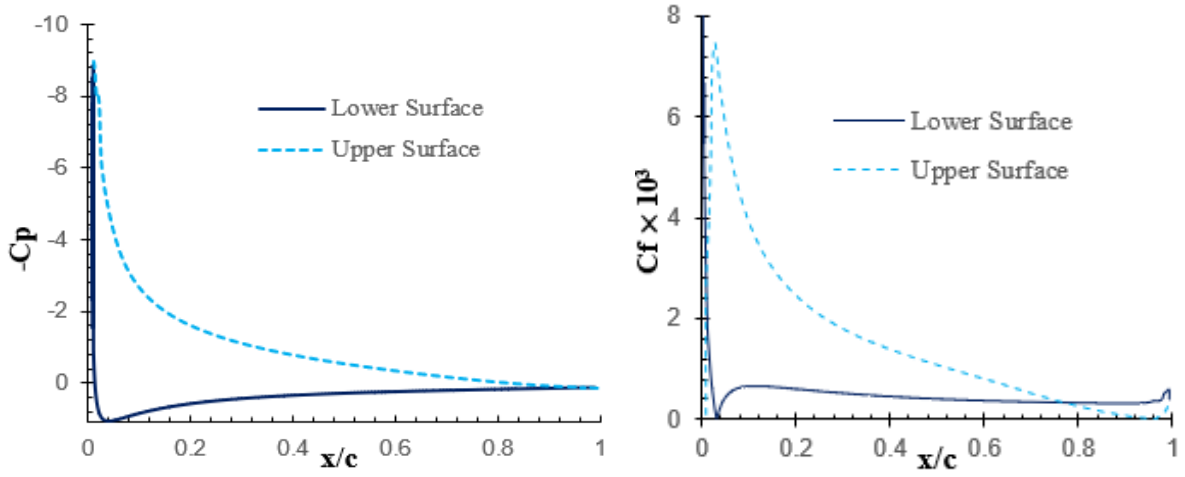

Figure 24: C_p and C_f for $\alpha = 14°$

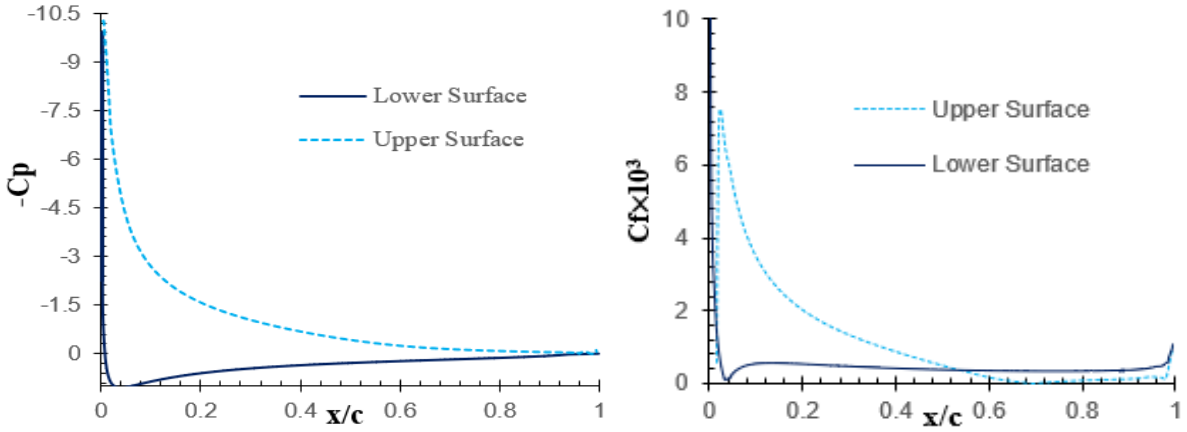

Figure 25: C_p and C_f for $\alpha = 16°$

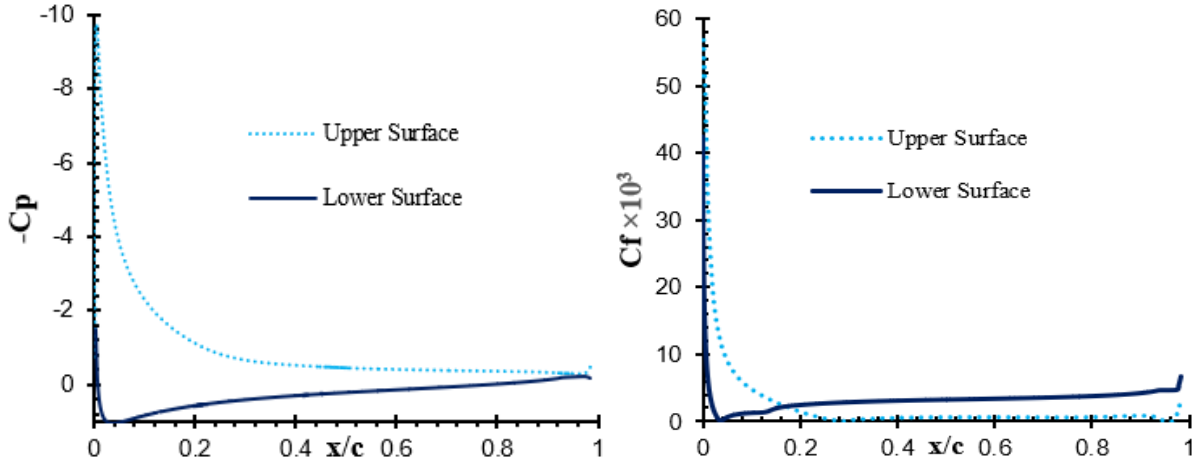

Figure 26: C_p and C_f for $\alpha = 18°$

As the AoA increases, until the airfoil is in full separation state, the suction peak is stronger and adverse pressure gradient not only occurs closer to the LE but is also more intense. The suction peak had a maximum (in magnitude) for the pre-stall case of 8.969, a maximum of 10.258 for the stall case and of 9.755 for the post-stall angle.

Strong adverse pressure gradient occurring earlier will lead to transition from laminar to turbulent regime occurring also earlier. For an AoA of $14°$, transition started at $x/c = 0.01$ and ended at $x/c = 0.030$, on the upper surface of the airfoil. For the stall AoA, transition started at $x/c = 0.01$ and ended at $x/c = 0.022$. The post-stall AoA, transition started at $x/c = 0.002$ and ended at $x/c = 0.005$. Meaning a 14.4% increase in suction peak from $\alpha = 14°$ to $\alpha = 16°$, did not influence the transition starting point. However, transition was completed 0.8% earlier on the upper surface. For the post-stall AoA, transition not only started earlier, but also ended faster. Although the suction peak is not stronger than the stall angle suction peak, the stall state (full separation on the upper surface), seems to lead to transition to turbulent regime occurring even earlier.

On the lower surface, as the AoA increased, transition point began to occur earlier. For AoA of $14º$, transition seemed to start at $x/c = 0.93$, while for the stall AoA, transition started at $x/c = 0.90$. In both cases, the skin friction coefficient plots did not verify the conclusion of transition.

C_f also gradually increases with a slight increase of the AoA from $\alpha = 14°$ to $\alpha = 16°$. When full separation occurs, the situation of post-stall, C_f increases immensely, with it is peak on the upper surface being higher than $C_f = 60 \times 10^{-3}$. Although C_f increases, the major component of the increase of C_d for this AoA is the pressure drag, $D_{pressure}$, which results from the pressure difference between the front and rear of the airfoil.

5.3 Dynamic stall

According to McCroskey [1] it is possible to distinguish two major categories of dynamic stall: light stall and deep stall. Light stall shares some of the general features of static stall, as lift loss, increase in drag and negative pitching moment, after some AoA is reached. However, it produces a major increase in the extent, severity and duration of the separation phenomenon. Deep stall occurs for higher AoA, with the passage of the vortex over the suction side of the airfoil producing values of lift, drag and moment coefficient far larger than the verified in static conditions. Also, large amounts of hysteresis occur during the cycle.

5.3.1 Light stall

The results presented here were obtained according to the following pitching motion equation:

$$\alpha(t) = 0.1702 + 0.1702\sin(3t) \tag{5.1}$$

which corresponds to $\alpha_{max} = 19.5°$ and $\kappa \approx 0.02$. According to Leishman [3], this reduced frequency would likely correspond to a quasi-steady flow. However, the obtained results point towards the conclusions of Digavalli [24], since clear unsteady behaviour was verified and although κ was small, the length-scale $\kappa\sqrt{Re_c} \gg 1$.

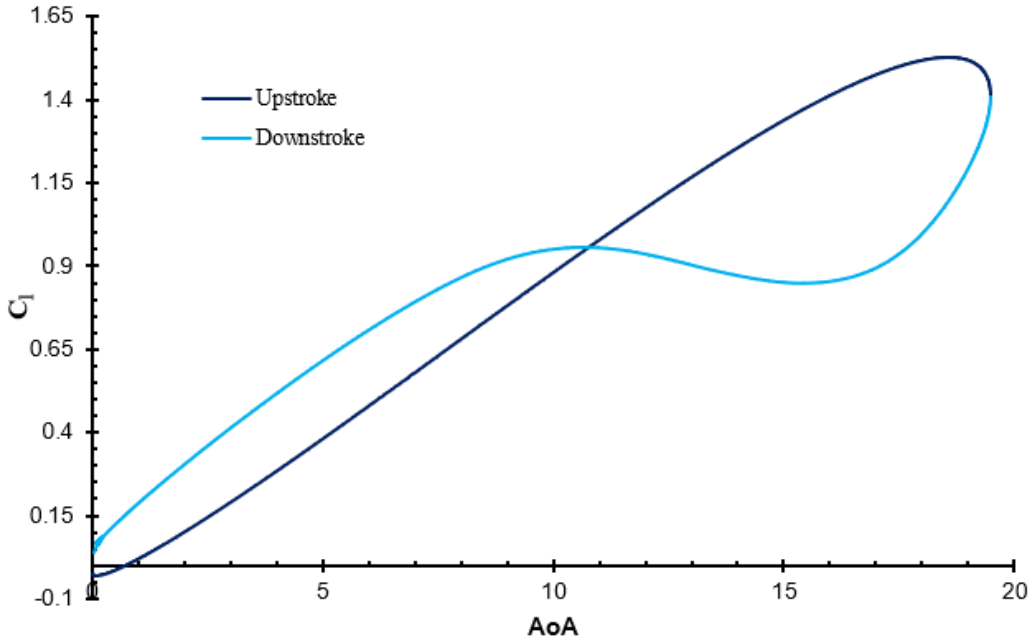

Figure 27: C_l for the light stall case

Several aspects of the obtained results must be discussed, namely: moment stall; delay of lift stall; no clear peak due to DSV; hysteresis format.

Static results pointed towards stall happening at $\alpha = 16°$ with $C_l = 1.440 \pm 0.0754$. In these dynamic conditions, for $\alpha = 16°$, $C_l = 1.411$, which first of all is similar to the static results and well inside its uncertainty range; second, stall does not happen for this AoA. In fact, lift stall only happens $2.6°$ later, for $\alpha = 18.6°$ with $C_l = 1.525$. Although lift stall happens, there is no visible peak in C_l from the DSV. Both Digavalli [24] and Choudhry [28] verified that for κ as small as $\kappa = 0.0095$ and $\kappa\sqrt{Re_c} > 2$, it was possible to obtain a lift peak due to DSV. However, both of these studies were done for low Re, between $5 \times 10^4 - 1 \times 10^5$. It becomes then unclear at what value of κ does the DSV start to evidence the peak in C_l vs α plot.

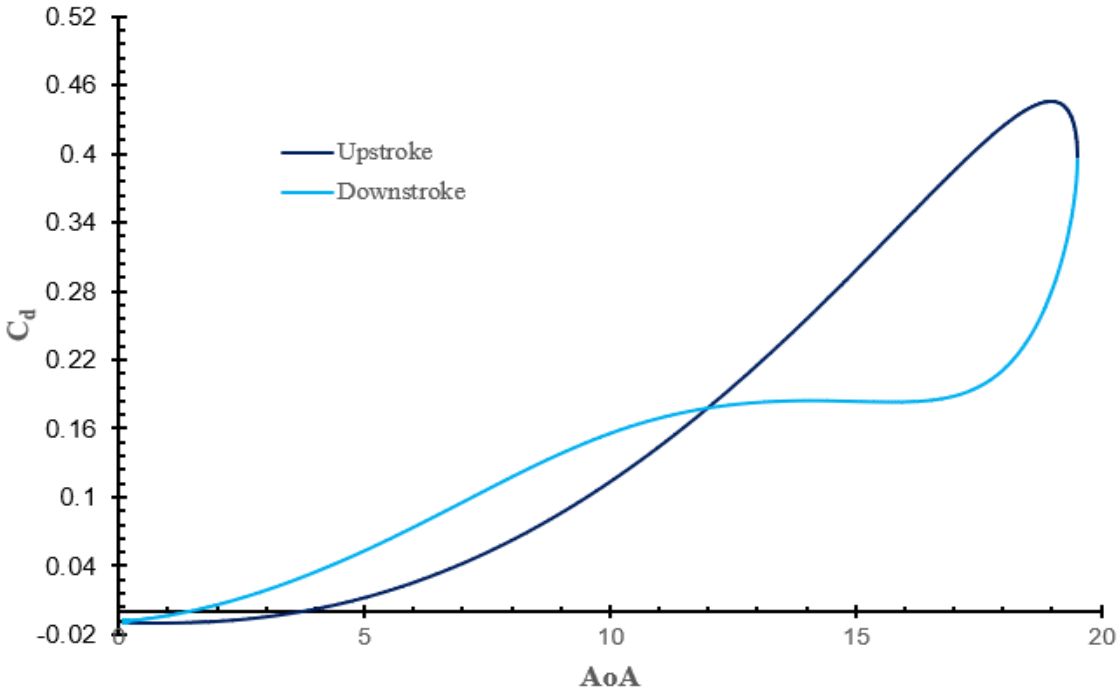

Figure 28: C_d for the light stall case

Since lift stall occurs for an AoA close to α_{max}, the airfoil begins the downstroke motion in lift loss, which leads to the type of curve seen in Figure 27, from $\alpha = 19.5°$ to $\alpha = 16°$. Both Leishman [3] and Carr [53] state that flow reattachment can take place if and when the AoA becomes low enough. However, there is a lag in this process due to the reorganization of the flow from fully separated until it becomes possible to reattach [54] and also because of the reverse kinematic of "induced camber" effect on the LE, due to the downstroke movement of the airfoil. Flow reattachment only occurs for AoA well below the static stall AoA. For this case, reattachment seems to occur for $\alpha = 10.8°$. Owing to these lags in the development of diverse flow states, a considerable amount of hysteresis is present.

The obtained values for C_d are much higher than the values for the steady case. This is the first major observation regarding drag in dynamic stall. On one hand, dynamic stall does allow for an increase in the attainable lift, however it comes not only at the cost of nose-down pitching moment and torsional loads, but also at the cost of increased drag. For $\alpha = 18.9°$, C_d is maximum, meaning it occurs slightly later than the lift stall, only $0.3°$ lag between the two. Moreover, when the flow is fully separated, the drag

starts to reduce and in addition to it, the airfoil begins the pitching down movement, leading to the hysteresis verified in Figure 28. Similar to the results of C_l, from $\alpha = 16º$, downstroke movement, the flow does seem to be "stabilizing" at $\alpha = 11°$, which is visible in the C_d plot.

Moment stall, which is very important when studying dynamic stall, since it is the diverging point of the pitching moment, happens at $\alpha = 17.9°$. Just like expected, the moment stall happens earlier than the lift stall, in this case, $\alpha = 0.7°$ lag. This moment stall, normally, happens at the onset of vortex shedding, whereas the lift stall happens when the vortex is moving across the upper surface and transitioning into the wake. This result indicates that the formation of DSV and its movement across the upper surface lasts only $0.7°$. From the moment stall AoA the airfoil begins a nose-down pitching moment. It reaches a minimum value of $C_m = -0.0342$ for $\alpha = 19.1°$, in the downstroke. The airfoil then begins its moment recovery and at $\alpha = 16.8°$ it closes the first loop. This loop is called a loop of negative damping. This comes from the torsional damping factor, which is positive when it corresponds to a counterclockwise loop in the C_m vs α plot and negative when is a clockwise loop [3].

As previously mentioned, the nonlinear loads obtained by operating the rotor in proximity to retreating blade stall, may introduce aeroelastic stability problems. One of these problems, also mentioned already, is stall flutter. Stall flutter occur when negative aerodynamic damping changes a stable aeroelastic blade into a high amplitude limit cycle oscillation. Light dynamic stall introduces a second loop, in this case of positive damping, so that the pitching moment curve looks like some form of a figure eight. For the studied conditions, the second loop is larger than the first one, meaning the net damping during the cycle is positive.

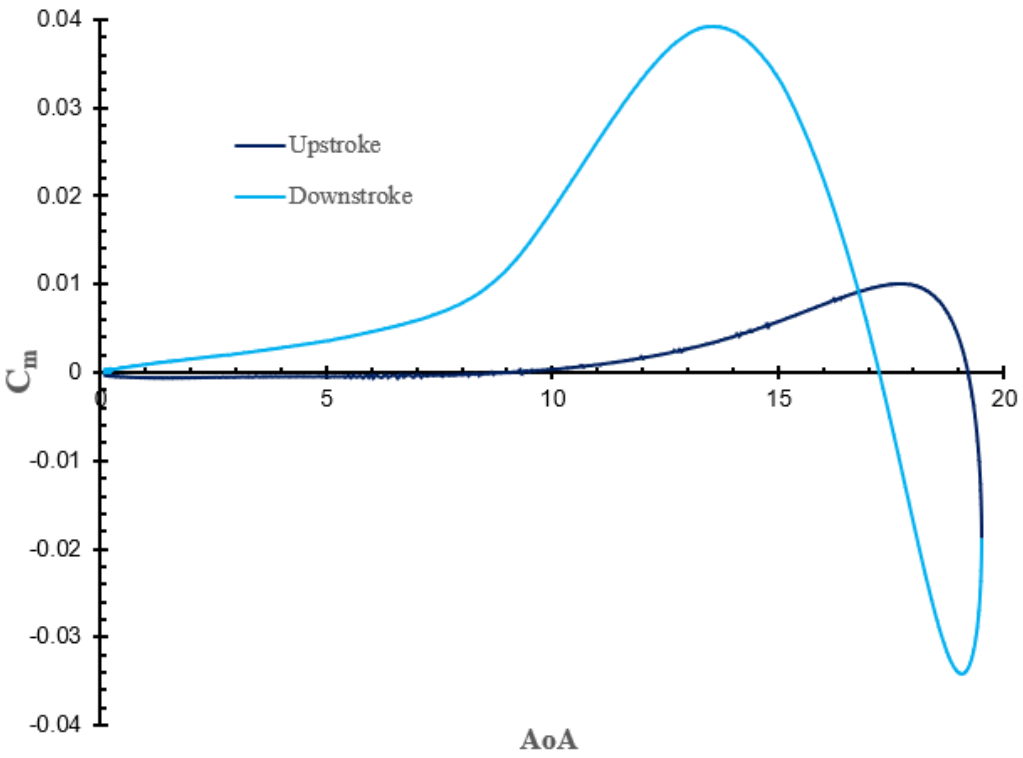

Figure 29: C_m for the light stall case

5.3.2 Deep stall

The results presented here were obtained according to the following pitching motion equation:

$$\alpha(t) = 0.288 + 0.1726\sin(15.18t) \tag{5.2}$$

which corresponds to $\alpha_{max} = 26.39°$ and $\kappa = 0.075$.

The study of deep stall is a complex one, due to the large separations observed, all the vortex interactions with the airfoil and with each other and the large amount of hysteresis obtained from all these. In order to facilitate its study and understanding of all the phenomena, Figure 33 presents the vorticity field around the airfoil, Figure 34 presents the $-C_p$ plot for some crucial AoA and Figure 35 presents the velocity field.

From the beginning of the cycle, $\alpha = 6.61°$, to approximately $\alpha = 20°$ the flow remains fully attached to the airfoil, which already represents the delay of lift stall to much higher AoA than the predicted static stall AoA ($\alpha = 16°$). From $\alpha = 20°$ to $\alpha = 22.2°$, the separated flow grows and already encompasses a large area of the upper surface, Figure 33(c). At $\alpha = 23.98°$, although not clearly visible from Figure 33(d), the DSV starts to get formed. Figure 34 also indicates it, given the high values (magnitude) of C_p at the LE of the airfoil. Furthermore, the vorticity of the TE wake also increases and is expected, at some later stages, to roll up and form the TEV. Also, one indication that the DSV at $\alpha = 23.98°$ is in the beginning of its formation, is the moment stall AoA. Looking at C_m it possible to verify it is constant until $\alpha = 20.5°$. From this point it starts to decrease slightly, however it does not seem to "diverge" which is Leishman's definition of moment stall [3]. One might say that this "divergence point" of C_m occurs between $\alpha = 23.5°$ and $\alpha = 25°$, which indicates that moment stall might not have occurred exactly when the DSV was formed, but when its size was enough for the suction over the upper surface to "break" the airfoil pitching moment.

At $\alpha = 25.0°$, DSV not only was large enough, as well as started its movement downstream. The lift overshoot resultant from it is clearly visible in Figure 30 and at this AoA, C_d starts to decrease. At $\alpha = 26°$, Figure 33(e) and Figure 34, DSV is already at $x/c = 0.6$. At this AoA, lift stall as still not occurred. Between $\alpha = 26°$ and $\alpha = 26.3°$ Figure 33(f), DSV is already at $x/c = 0.8$ and the boundary layer at the LE is quite unstable, given that part of the DSV broke into two smaller counter-rotating vortices. In addition, the vorticity field of the TE wake is also stronger. Lift stall finally occurs between these two AoA and C_m registers the minimum value of nose-down pitching moment, for the upstroke motion.

As soon as the downstroke motion begins, Figure 33 (g), C_l decreases rapidly and C_m increases. DSV is also completely convected and appears to be almost completely separated from the airfoil. TEV, that has penetrated from the pressure side of the airfoil into the suction side, has been initiated [55], with its vorticity also being higher. At the same time, the two vortices at the LE are growing in size. The interaction between the TEV and the DSV is complex and seems to occur during the period in which TEV is still growing and DSV is already detached from the airfoil. This interaction leads to another decrease in C_l followed by a very strong nose-down pitching moment, which results in the minimum value of $C_m = -0.955$. The TEV is continuously growing in size and strength, originating a strong nose-up pitching motion on the airfoil, reason why C_m starts to increase rapidly.

At $\alpha = 24.4°$,of the downstroke motion, the pair of vortices on the LE due to their size, joined together into one larger and stronger vortex, dominating the suction side of the airfoil. According to Leishman [3], this is the secondary vortex, which is the reason to a significant increase in C_l during the downstroke motion, as well as strong nose-down pitching moment which leads to another decrease in C_m. The TEV is now much bigger and its vorticity is also much higher than before.

At some point, approximately $\alpha = 24°$, it is possible to see from C_l and C_m, Figure 30 and Figure 32, that C_l starts to increase again and C_m starts to decrease again with strong nose-down pitching motion. This is mainly due to two reasons: the TEV detaches and the new LEV is strong enough to cause another lift overshoot and nose-down pitching moment.

For $\alpha = 22.2°$, the LEV is now being convected downstream the suction side and its magnitude is lower. Given this, C_l reaches its third peak and starts decreasing, while, as expected, C_m reached its third peak in negative pitching moment and starts to increase. From Figure 33(i) and Figure 35(e), two important detail must be noted: a new vortex is starting to from at the LE and at the same time, a second rolling-up vortex is starting to form at the TE. However, both of these vortices are now much weaker than the previous ones, reason why their impact in the aerodynamic coefficient is smaller.

This is a repetitive phenomenon, the formation of a LEV and the rolling-up at the TE, forming a TEV. For $\alpha = 20.6°$ and $\alpha = 17.5°$ is also possible to see the convection of former vortices, the formation of a new vortex at the LE and the roll-up at the TE.

Eventually all the vortices are convected to the wake and flow starts to reorganize. It takes a longer time to it, than for example in the light stall case. Reason why during the cycle reattachment after flow separation does not occur, until the minimum AoA of the cycle.

Deep stall simulations were not easy, computationally and also comparison with data for similar parameters. Although for angles not high as the tested, [55] obtained similar results and conclusions for the deep stall case, with the formation of secondary vortices and even, as was the case here, more vortices after it, until the flow had stabilized and the airfoil was at low AoA.

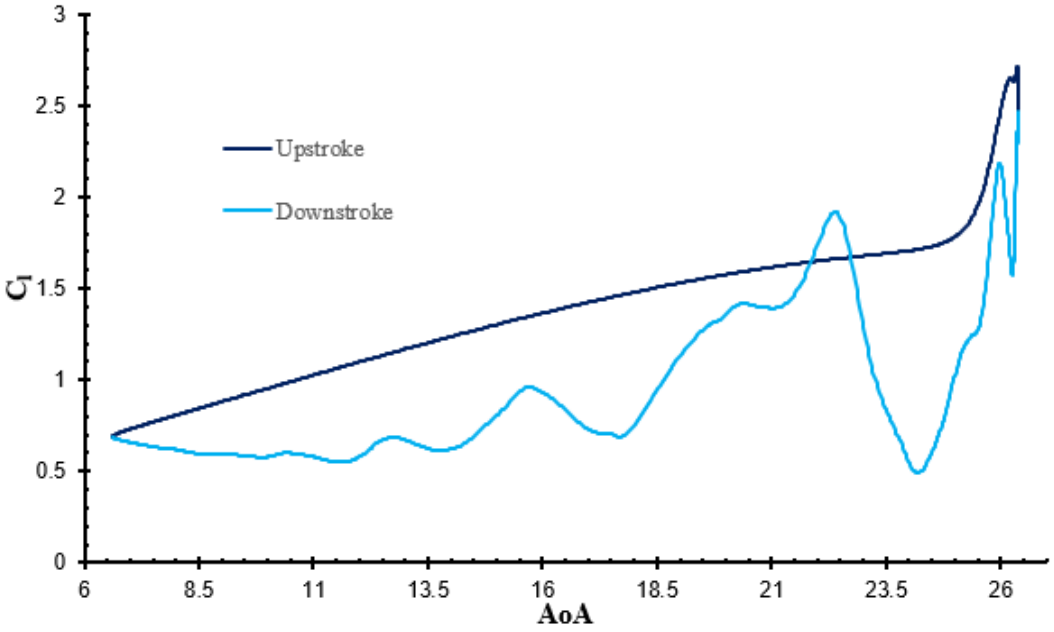

Figure 30: C_l for the deep stall case

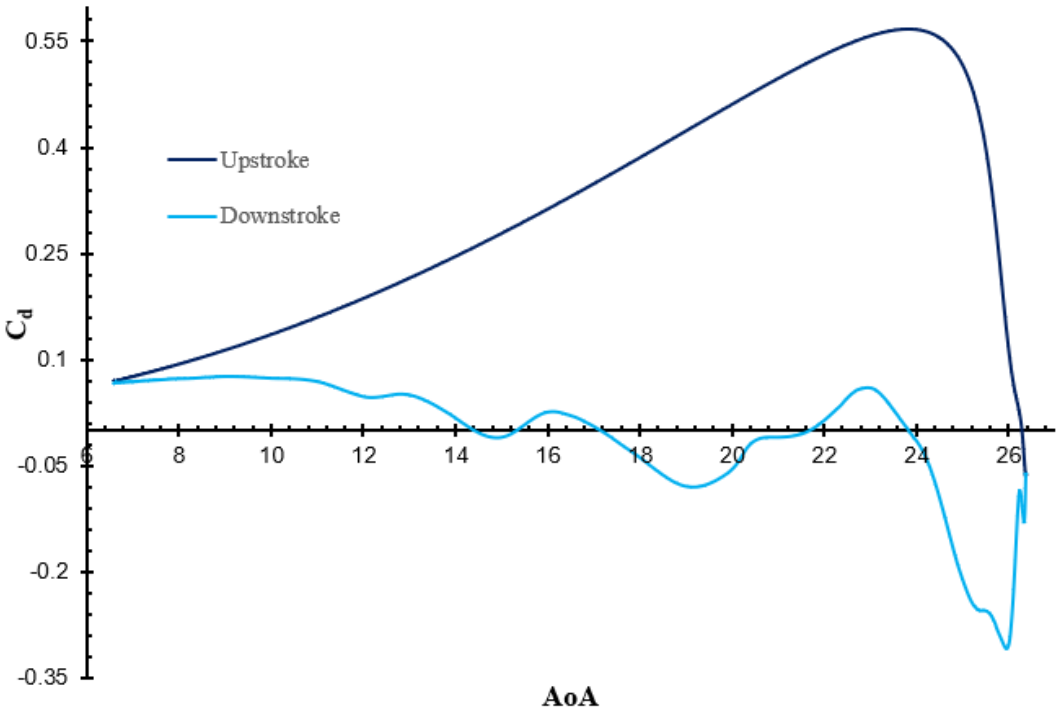

Figure 31: C_d for the deep stall case

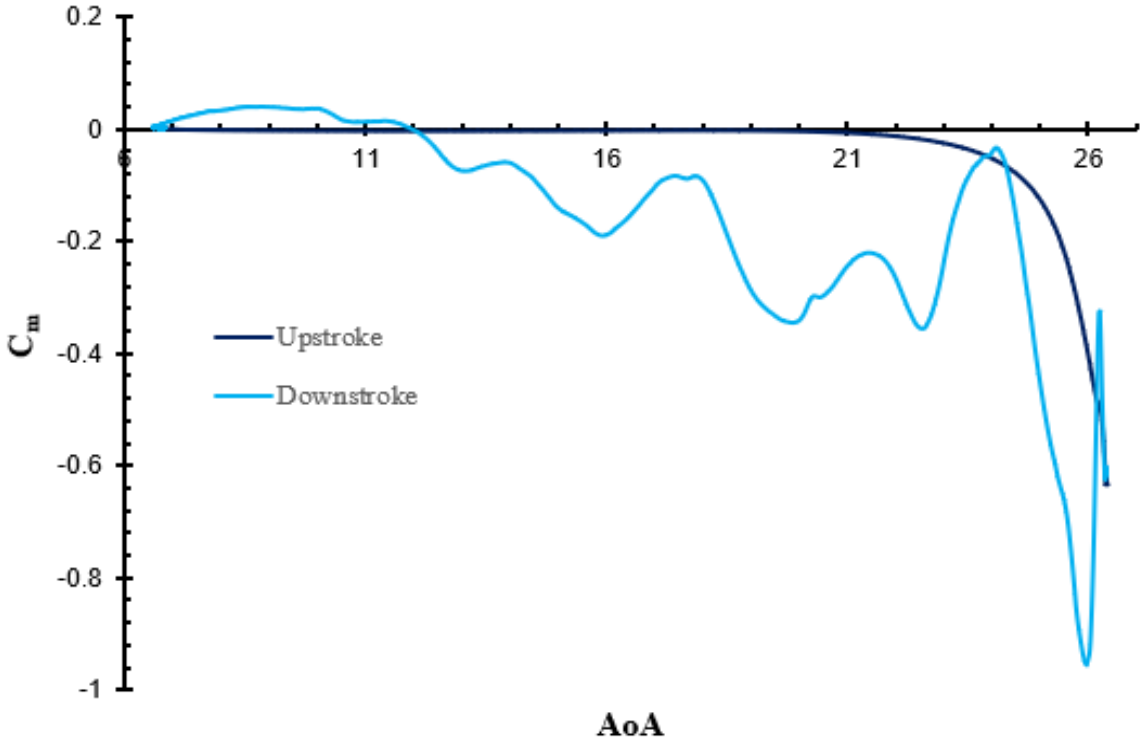

Figure 32: C_m for the deep stall case

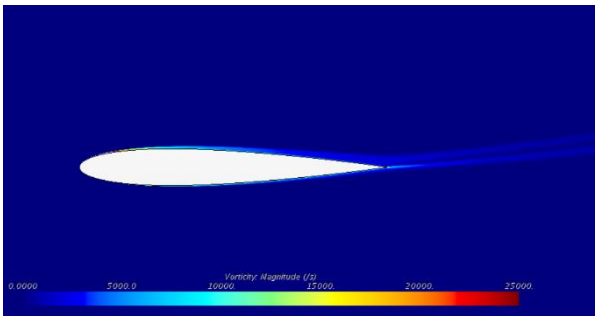

a) $\alpha = 10° \uparrow$

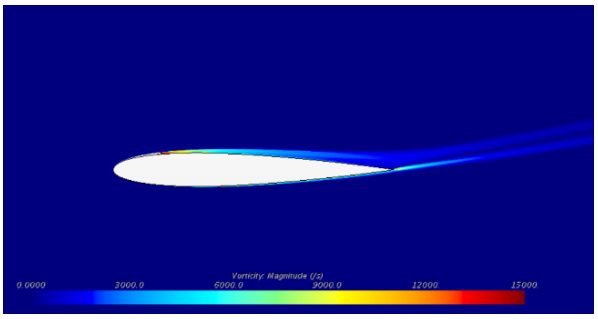

b) $\alpha = 16° \uparrow$

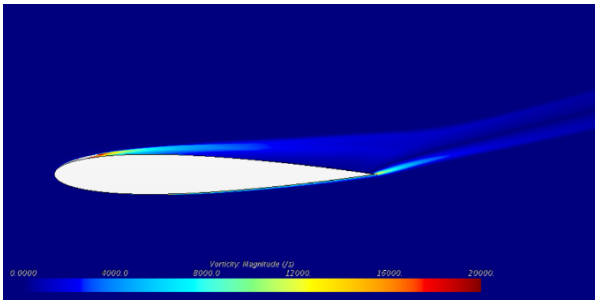

c) $\alpha = 22.2° \uparrow$

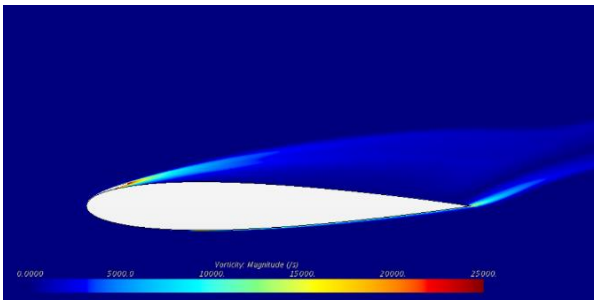

d) $\alpha = 23.98° \uparrow$

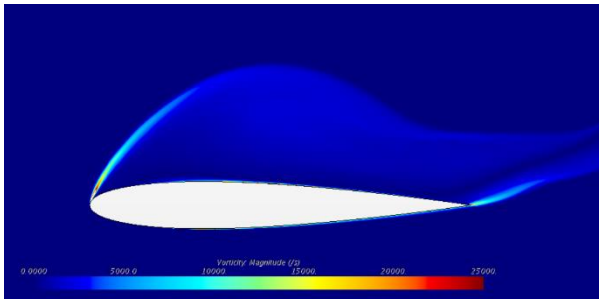

e) $\alpha = 26° \uparrow$

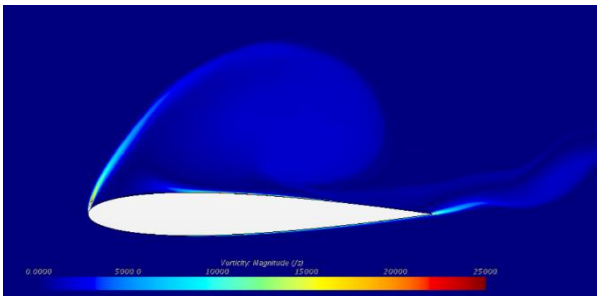

f) $\alpha = 26.3° \uparrow$

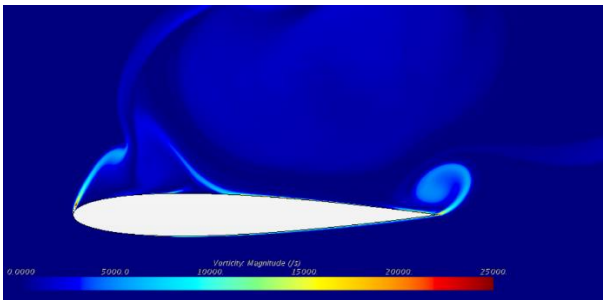

g) $\alpha = 26.27° \downarrow$

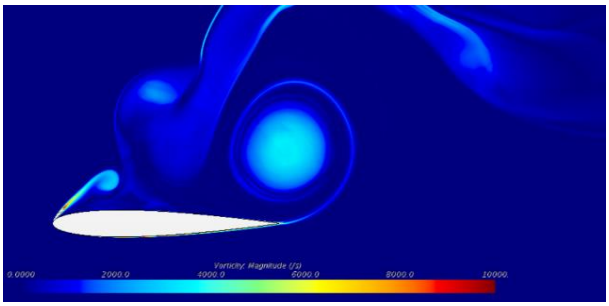

h) $\alpha = 24.4° \downarrow$

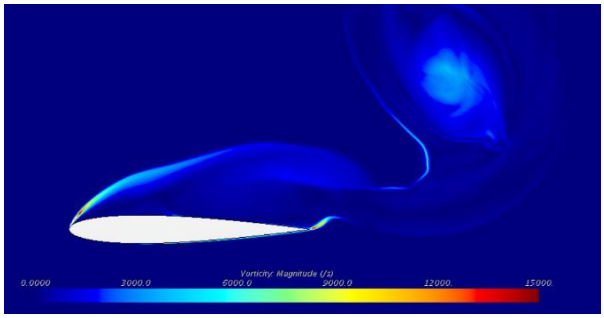

i) $\alpha = 22.2° \downarrow$

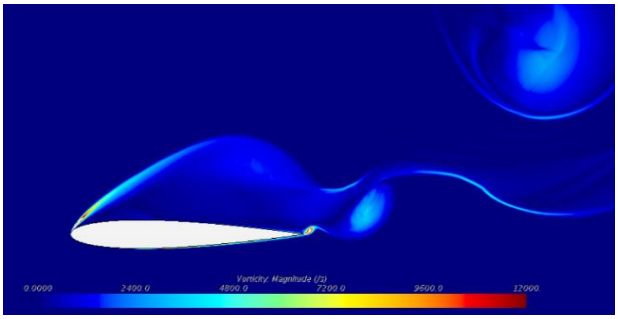

j) $\alpha = 20.6° \downarrow$

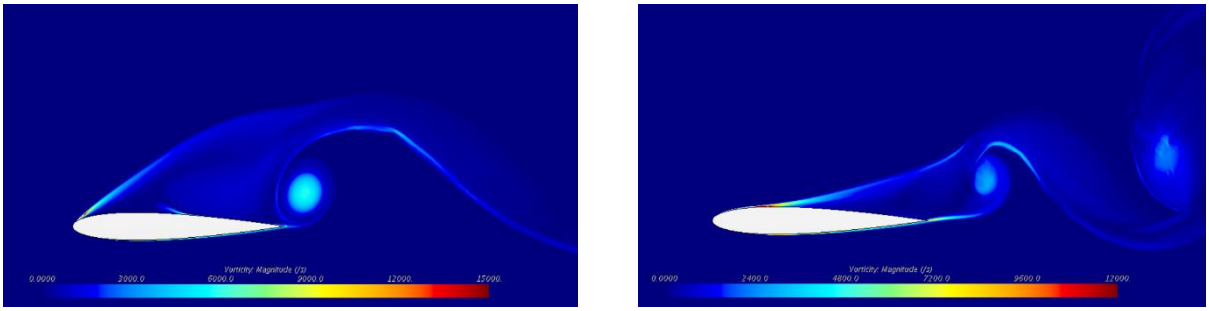

k) $\alpha = 17.5° \downarrow$ l) $\alpha = 10.8° \downarrow$

Figure 33: Vorticity field for the deep stall case, with ↑ indicating upstroke and ↓ indicating downstroke

Regarding C_d is also important to take a closer look to its values. First of all, and as expected, the maximum C_d is higher than the higher C_d for the light stall case, since higher AoA are achieved.

After lift stall occurs, the drag reduction is very abrupt and C_d is negative at the end of the upstroke motion. With the beginning of the downstroke motion, C_d reduces even more and its minimum value is $C_d = -0.31$. As seen in the static stall analysis, the medium mesh (and even the fine mesh) did demonstrate some difficulties in predicting C_d during post-stall situation. In fact, in all deep stall dynamic simulations performed during this works' duration, C_d was always the most difficult aerodynamic coefficient to compare with any kind of experimental or computational data from other authors. Future work can be done with finer meshes regarding deep stall simulations, to evaluate C_d and compare with the results from this work.

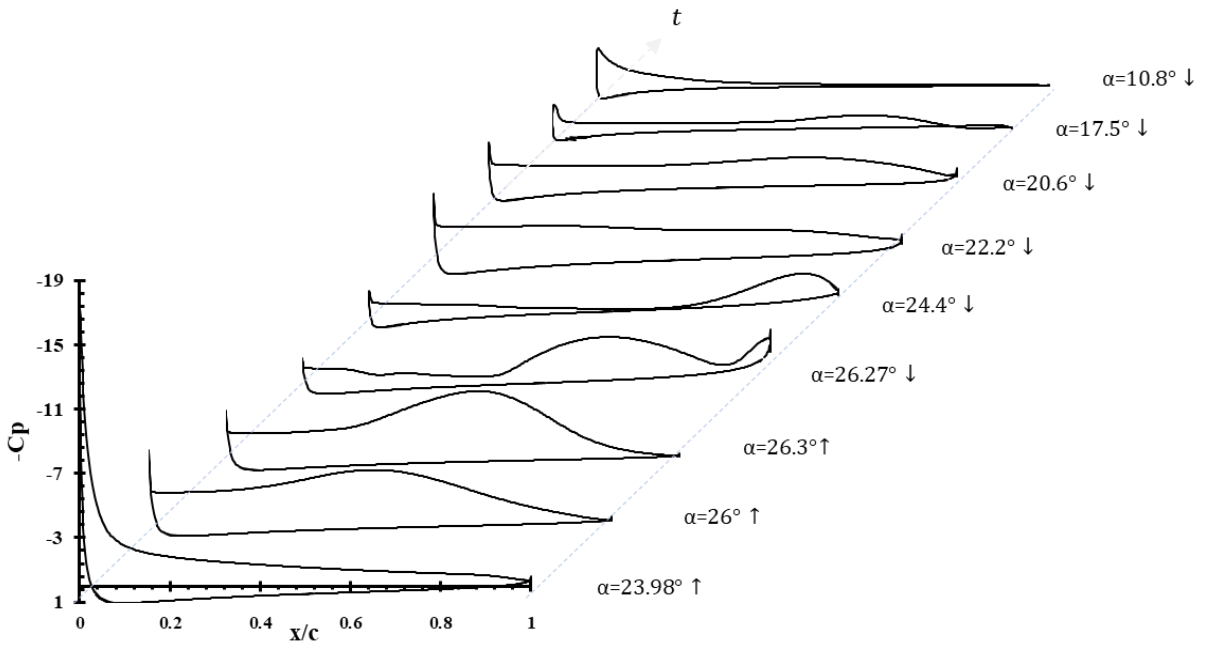

Figure 34: $-C_p$ plot for some AoA during the cycle of the deep stall case, with ↑ indicating upstroke and ↓ indicating downstroke

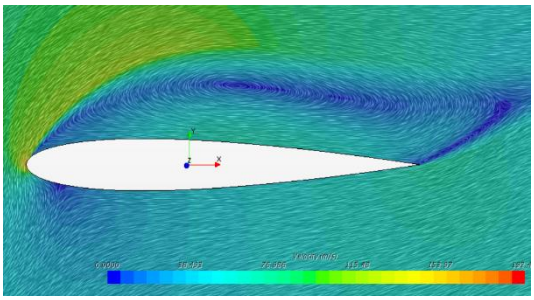

a) $\alpha = 26° \uparrow$

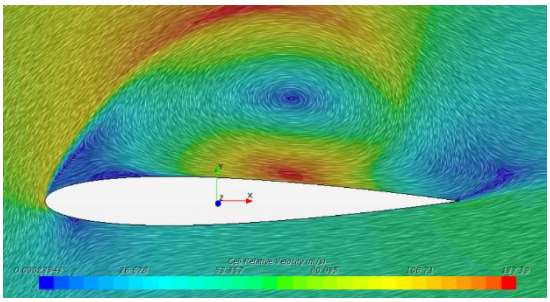

b) $\alpha = 26.3° \uparrow$

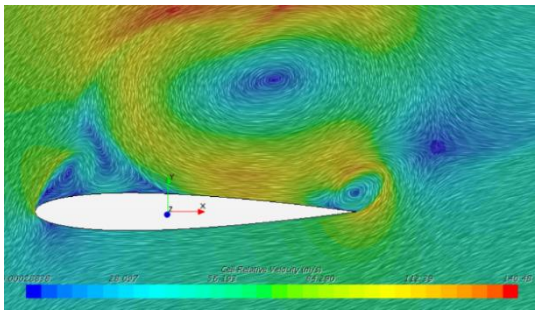

c) $\alpha = 26.27° \downarrow$

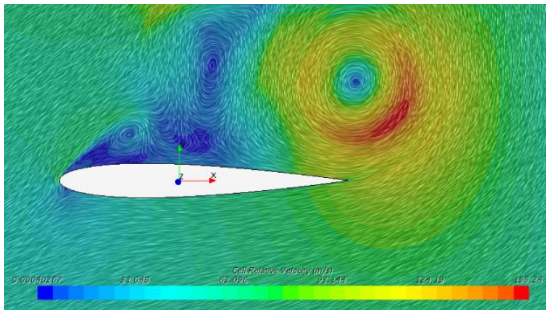

d) $\alpha = 24.4° \downarrow$

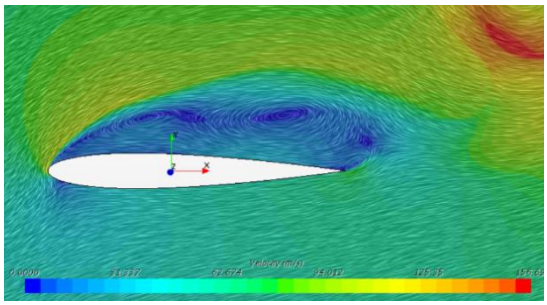

e) $\alpha = 22.2° \downarrow$

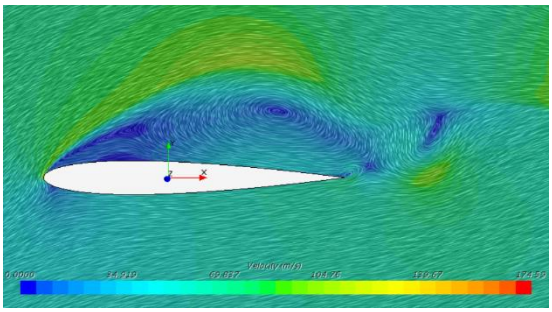

f) $\alpha = 20.6° \downarrow$

Figure 35: Velocity field for some AoA during the cycle of the deep stall case, with ↑ indicating upstroke and ↓ indicating downstroke

5.3.3 Effect of κ

In section 2.3.1 was presented what happens, in theory, when κ changes to the aerodynamic coefficients of a pitching airfoil. With that as a goal, it was simulated the pitching motion with different values of κ. Figures 36,37 and 38 are the aerodynamic coefficients for the following two pitching motions:

$$\alpha(t) = 0.1702 + 0.1702\sin(3t) \tag{5.3}$$

$$\alpha(t) = 0.1702 + 0.1702\sin(11.7t) \tag{5.4}$$

Corresponding, respectively, to $\kappa = 0.02$ and $\kappa \sim 0.07$. Both cases lead to light stall type.

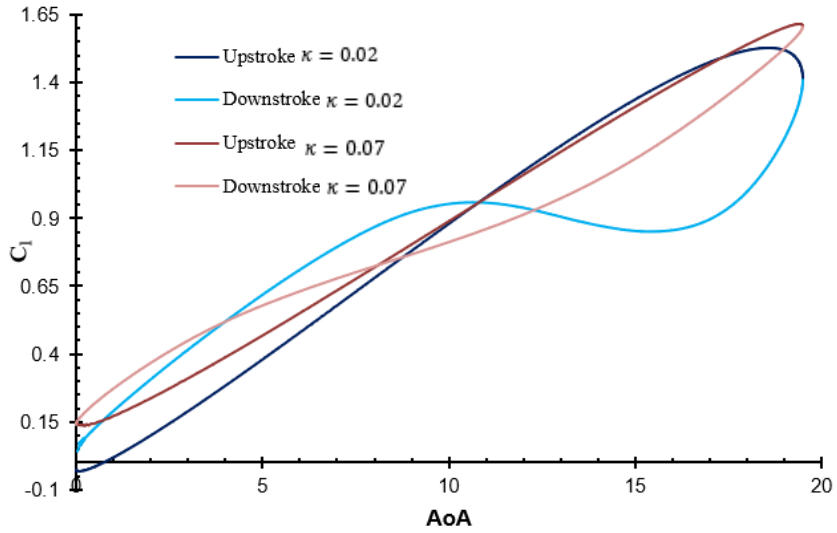

Figure 36: Comparison of C_l for different values of κ

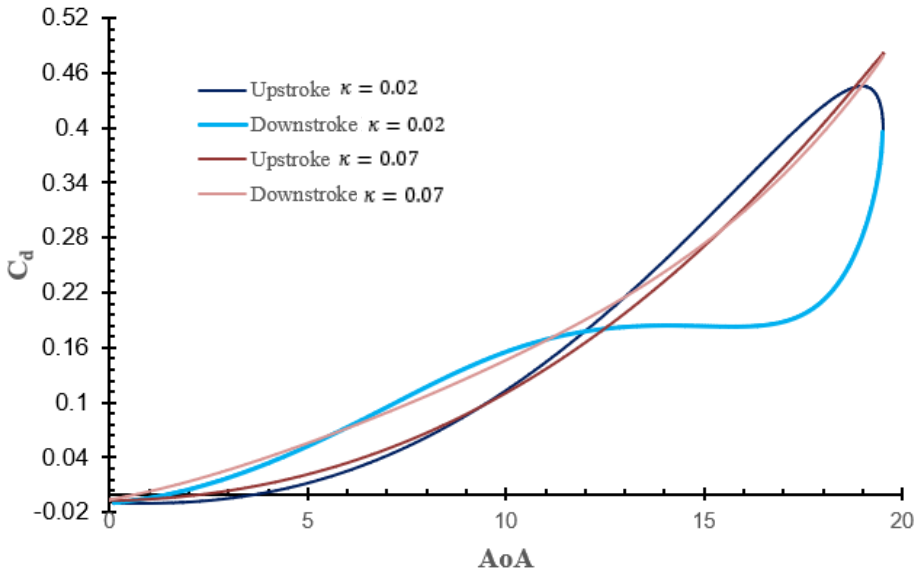

Figure 37: Comparison of C_d for different values of κ

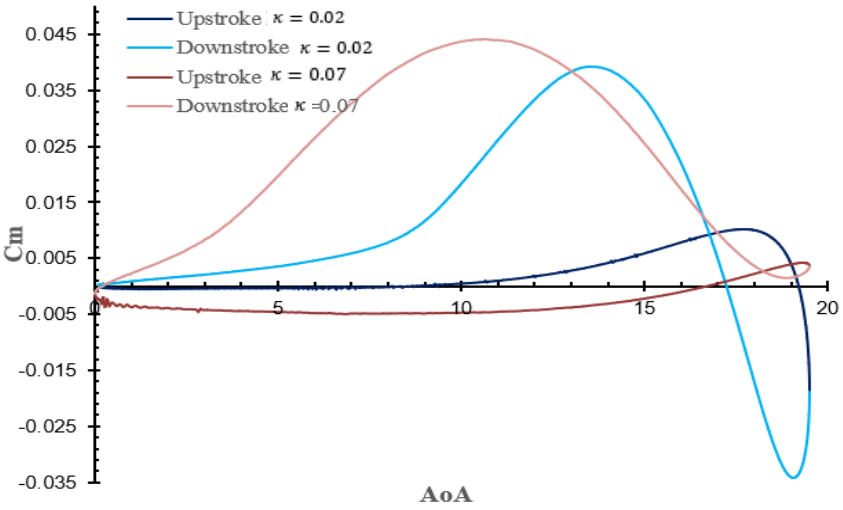

Figure 38: Comparison of C_m for different values of κ

The analysis of the obtained coefficients for the first case, $\kappa = 0.02$ can be seen in section 5.3.1. The Figures above show the powerful effect of reduced frequency on both C_l, C_d and C_m. It is expected that increasing κ the onset of flow separation is delayed to even higher AoA and also delay the AoA at which the flow reattachment occurs.

The first result of interest is, in fact, the delay of flow separation for higher AoA. For the case $\kappa = 0.07$, flow separation occurs at $\alpha = 19.5°$ which is the maximum AoA achieved in the cycle. Not only did it delay the flow separation, as the corresponding C_l is also higher. $C_l = 1.607$ for $\alpha = 19.5°$, whereas the case with $\kappa = 0.02$ had a maximum C_l for $\alpha = 18.6°$, $C_l = 1.525$ and for $\alpha = 19.5°$, since the flow was already fully separated, $C_l = 1.407$. Leishman [3] attributes these results to the kinematic effect of "induced camber", that progressively lessens the leading edge pressure gradients, for a given value of C_l, and thus flow separation is delayed to higher AoA. Furthermore, higher κ leads to smaller hysteresis, and for some values, even might prevent flow separation for occurring, meaning no hysteresis would be obtained, see Figure 39.

Flow reattachment, as expected, also seems to occur later in the cycle. For $\kappa = 0.07$, reattachment apparently occurs for $\alpha = 8.05°$, a difference of $2.7°$ relatively to the smaller κ case and far inferior to its static stall angle. One of the reasons might be the higher frequency at which the airfoil pitches down, leads to an increased lag in the flow reorganization from fully separated, until it is able to reattach.

Furthermore, the value of C_l in the beginning of the cycle, $\alpha = 0º$, is much higher than the static case and then for $\kappa = 0.02$. This indicates that the rapid pitching motion, does not give the flow enough time to be completely organized around the symmetrical airfoil.

One drawback of the augmented C_l and delay of flow separation is that C_d is also higher for $\kappa = 0.07$. Also, the AoA at which the downstroke C_d is higher than the C_d for the upstroke occurs earlier and no visible plateau occur in the entire plot.

Moment stall, for $\kappa = 0.07$ occurs at α_{max}, which coincides with the lift stall AoA. The lag between these two phenomena is then equal to 0. This is, of course, due to the delay on the onset of flow separation, meaning the vortex shedding is also delayed and, in this case, given the small decrease in C_m during the negative damping loop, is weak. The airfoil is faced with weak nose-down pitching moment.

In addition, the loop of negative damping is much smaller than the correspondent for $\kappa = 0.02$, while the loop of positive damping is larger, *i.e.* net damping is positive during the cycle.

All these factors indicate that for κ as small as $\kappa = 0.07$ flow separation is almost avoided and the effect of negative damping also. One might then assume that for even higher values of κ, say a very unsteady flow with $\kappa \sim 0.2$, flow separation can be completely avoided.

Presented below is the same pitching motion as previously, but now with $\kappa = 0.198$, this is:

$$\alpha(t) = 0.1702 + 0.1702\sin(33t) \tag{5.5}$$

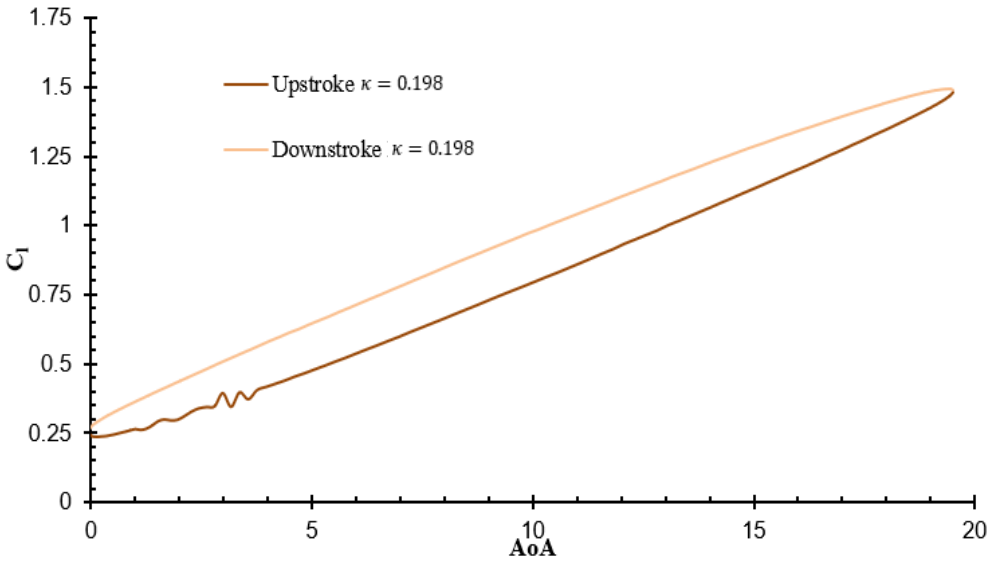

Figure 39: C_l for $\kappa = 0.198$

The results for $\kappa = 0.198$ agree with what was expected for a value of κ as high as the tested. Flow separation is completely avoided, with C_d not decreasing due to flow separation or C_m not having any sign of moment stall. C_l is now a hysteresis without any loops, with the downstroke motion having higher values of C_l than the upstroke motion, for the same AoA. This can also be seen in C_d, with the downstroke motion presenting higher values than the upstroke motion.

In terms of C_m, moment stall was completely avoided, also meaning that no negative damping loop was obtained, nor does C_m look like a figure eight.

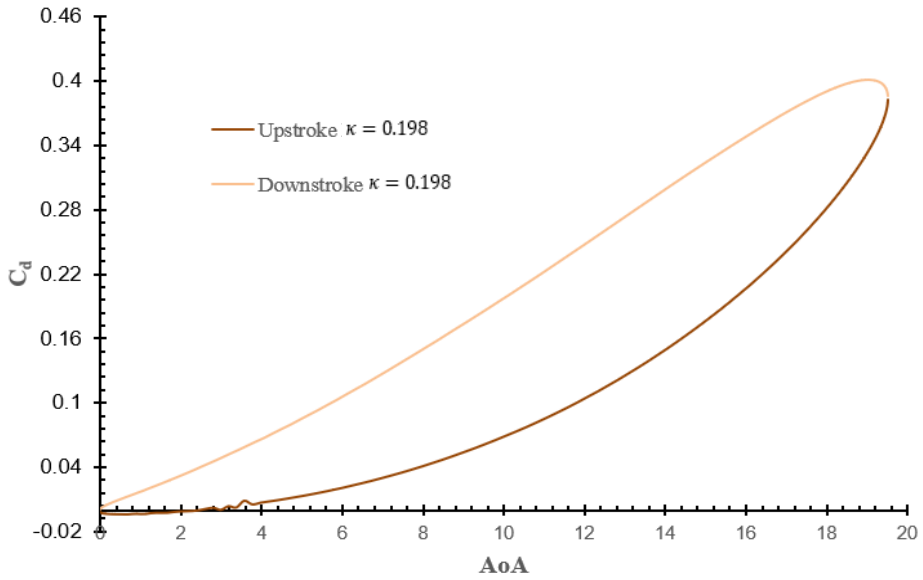

Figure 40: C_d for $\kappa = 0.198$

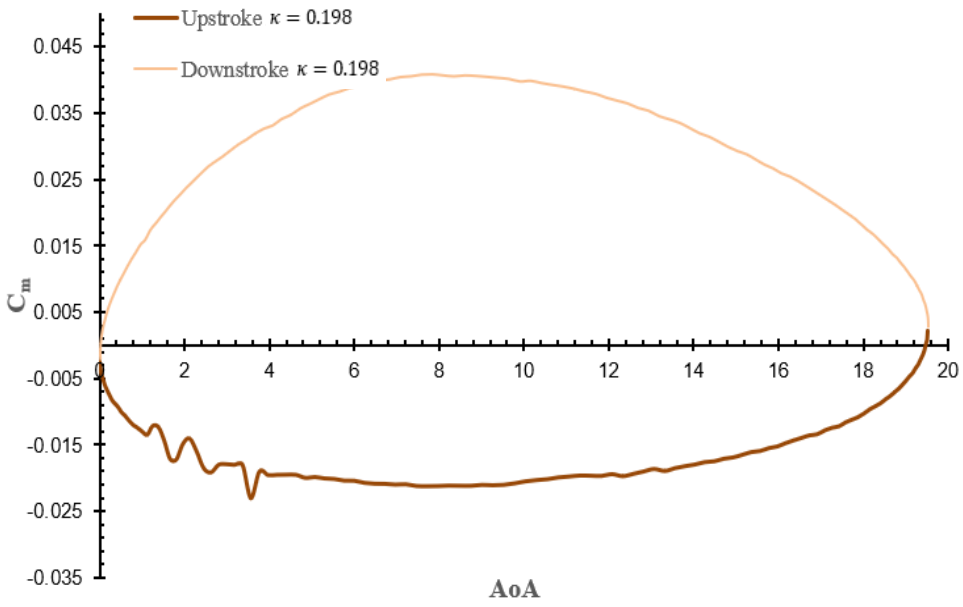

Figure 41: C_m for $\kappa = 0.198$

5.3.4 Effect of Re

As it was already stated in section 2.2.2, an increase of Re is believed to not have a major effect in an airfoil in a state of dynamic stall. Several studies have been conducted that led to that conclusion [30], [31], [29]. However, one might argue that all these studies have been done for relatively low Re $10^3 - 10^5$. A helicopter in forward flight might experience Re much higher than these values. An extensive study from NASA [56] did study the effect of various parameters in the dynamic stall process of some airfoils, including the NACA 0012. For R_e as high as 3.5×10^6, although with some differences, led to the conclusion of Re not playing a major role in the dynamic stall.

Having in mind that one of the major limitations of this study is neglecting compressible effects, it was attempted to study the effect for Re even higher than those studied by McAlister et al. [56]. For this, a simulation with $Re = 4 \times 10^6$ was performed. The results are presented below and compared with the results obtained from Equation 5.4. It is also important mentioning that changing Re, in this case, meant increasing the flow velocity. However, κ is also dependent of the flow velocity. So, in order to study the effect of Re and keep κ the same, w had to be changed in accordance.

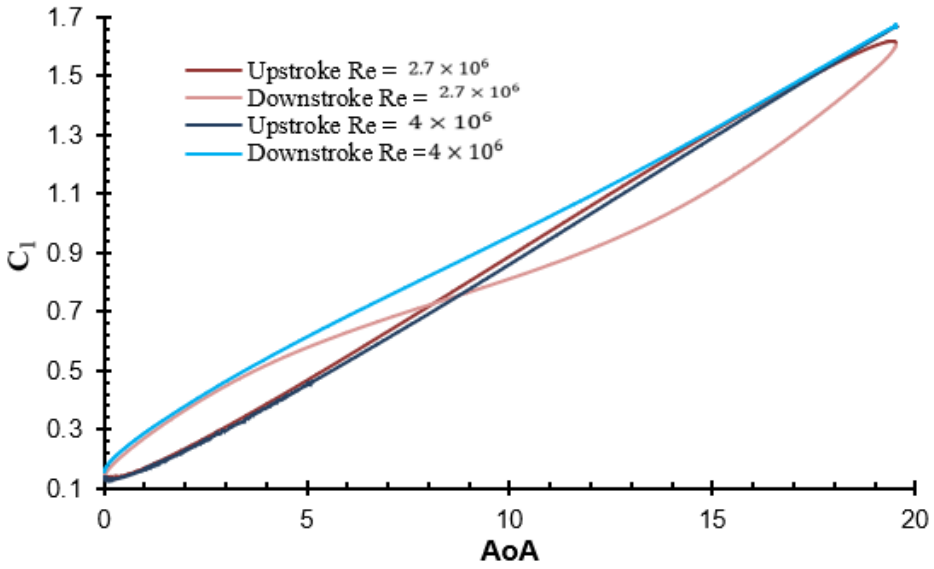

Figure 42: C_l for different values of Re

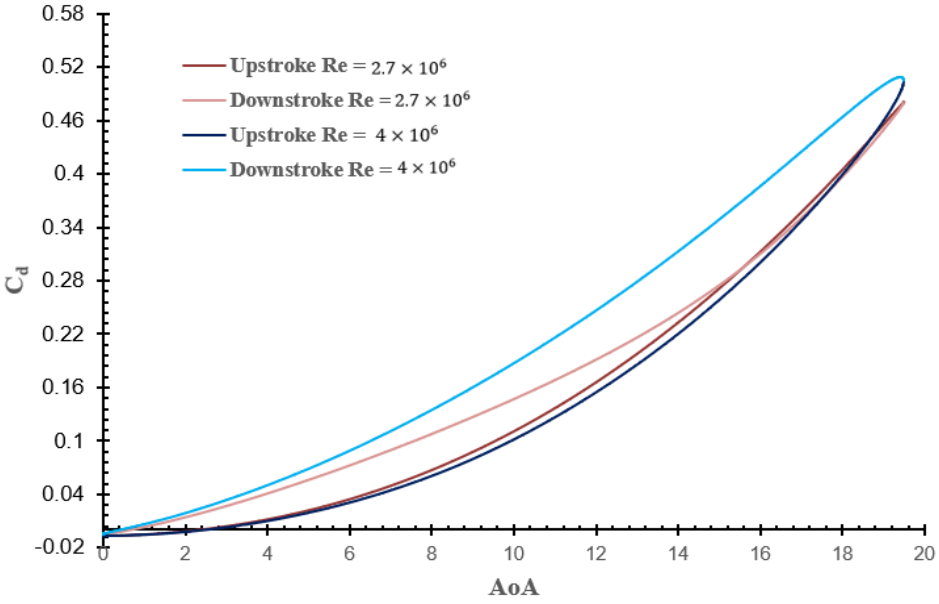

Figure 43 C_d for different values of Re

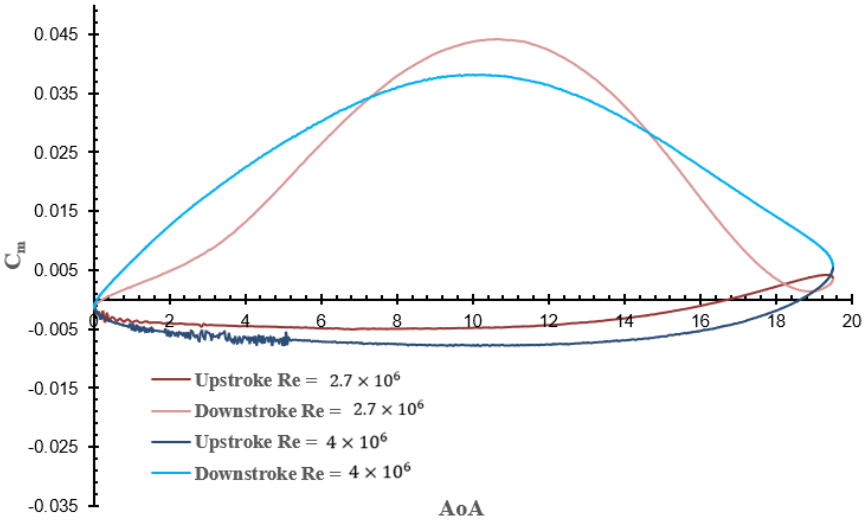

Figure 44: C_m for different values of Re

From the Figures above it is possible to infer that the obtained results show that dynamic stall is highly dependent on the Re, for high values of Re. Before analysing the results, care must be taken, since at the LE of the airfoil, the velocity was, for high AoA, equal to 300 m/s, or $M_\infty = 0.88$. This indicates that treating this problem as incompressible might lead to erroneous results and conclusions.

In the coefficients presented in the Figures above, the upstroke results agree very well for both cases, with C_m being the exception. C_l and C_d, for the higher Re case, are higher for maximum AoA with no flow separation occurring, which is the first major difference between both cases. During downstroke motion, no loop is verified for both C_l and C_d, with C_l for the downstroke motion being very similar to C_l

of the upstroke motion. The corresponding values of C_d of the downstroke motion are also higher than the values of C_d for $Re = 2.7 \times 10^6$.

In terms of C_m, moment stall did not happen, with no loop of negative damping occurring. As the airfoil starts its downstroke motion C_m starts to increase, since no vortex was formed at the LE (or was really weak), as the motion begins, the center of pressure dislocates and C_m increases. Reason why there is only a loop of positive damping.

These results might lead to the conclusion that Re indeed is of major importance for dynamic stall process. Further work has to be done in order to study the influence of high Re in the dynamic stall process. The author hopes these results can then be compared with future results, obtained from compressible flow simulations.

Chapter 6

Conclusions

6.1 Contributions

In the beginning of this work, the objectives were laid out and the author was able to fulfil them. Some results revealed to be very interesting, like the deep stall case, and others, like the influence of Reynolds number in the dynamic stall process, wait for future works to use them as comparison and evaluate their accuracy.

In terms of mesh refinement, some computational restrictions were imposed during this work's development. Unfortunately, the utilized mesh for dynamic simulation had only 3.5 million cells. Ideally a more refined mesh would have been used. However, a mesh with this density (designated in this work as medium mesh) revealed to predict steady stall AoA pretty accurately, as well as C_l and C_m. C_d was not easy to obtain good results in post-stall situation. Even with a finer mesh, it was not possible to completely obtain results inside the uncertainty range when comparing with experimental results.

After the selection of the mesh and its use on obtaining steady state results, light stall cases were simulated. Light dynamic stall maintains some characteristics of the static stall, however it presents some of the dynamic stall characteristics also like: stall onset delay to higher AoA; lift overshoot; Lift stall and momentum stall. In order to study this case, the selected pitching motion had $\alpha_{max} = 19.5°$ and $\kappa = 0.02$. A reduced frequency as low as this might be considered in the quasi-steady flow range. However, the results point towards the conclusion of Digavalli [24], meaning that the length-scale $\kappa\sqrt{Re_c}$ being much higher than 1 is a clear indication of unsteady behaviour.

Stall onset was delayed in $2.6°$, with C_l much higher than the maximum C_l of the steady stall case. This was a clear evidence of lift overshoot provided by dynamic stall. No lift peak resultant from DSV was verified. Furthermore, flow reattachment was verified, but only for much smaller AoA than the steady stall AoA. This is attributed to the lag in flow reorganization after flow separation and because the effect of the downstroke movement of the airfoil. The obtained values for drag were also much higher than the values for the steady case. Even though it is possible to obtain lift overshoot, it comes at a price: increased drag. Large hysteresis was present in both C_l and C_d plots. Moment stall was verified and occurred at $\alpha = 17.9°$, which correspond to lift stall having $0.7°$ lag between lift stall and momentum stall. Two loops were possible to verify in C_m plot, with the first being of negative damping and the second (much larger than the first) being positive, meaning the net damping during the cycle was positive.

For the deep stall case, where DSV formation and propagation across the upper surface is much more evident, a pitching motion with $\alpha_{max} = 26.39°$ and $\kappa = 0.075$ was selected. The flow remained fully attached to the airfoil until $\alpha = 20°$. The DSV started to from at $\alpha = 23.98°$, also possible to verify from

moment stall occurrence. At $\alpha = 25°$, DSV was large and was moving across the upper surface, with the resultant lift overshoot clearly visible from C_l pot. Lift stall finally occurred between $\alpha = 26°$ and $\alpha = 26.3°$, with the boundary layer being very unstable, leading to part of the DSV to degenerate into two smaller vortices. During this, the vorticity at the TE was growing stronger. As the downstroke motion begins, DSV is completely convected, the TEV has penetrated into the suction side and the two vortices at the LE are growing. The interaction between DSV and the TEV leads to a reduction in C_l and strong nose-down pitching moment. The pair of vortices then joined together and form what is called the secondary vortex. This results in an increase in C_l and reduction of C_m. The dynamic of TEV detachment and the new LEV being stronger lead to another lift increase and nose-down pitching moment reduction.

This dynamic of roll-up wake at the TE and formation of LEV is verified until late in the cycle, with each one of these pairs being weaker than the former pair. Reattachment never occurs during the cycle. For C_d it was, as expected, difficult to obtain good results.

Interesting results were also obtained varying the value of κ. As κ increases, flow separation is delayed to even higher AoA and flow reattachment delayed to further in the cycle. However, increased drag was also verified. The loop of negative damping was much smaller than the light stall case and the positive loop larger. The flow separation delay might be attributed to the kinematics of induced camber resultant from the pitching motion. This led to the conclusion that further increases in κ would lead to smaller hysteresis and even prevent flow separation, in some cases. This was verified when κ was increased from 0.07 to 0.198, leading to C_m not having signs of moment stall and C_l and C_d being hysteresis without any loops, whose downstroke motion values were higher than the values of upstroke motion.

As for the Re influence, the results contradict what was expected to happen. This might be attributed to the fact that high transonic flow was verified at the LE, meaning that incompressible flow models might lead to erroneous results. In any case, the results did indicate that Re was of very importance for the phenomenon, with the upstroke motion agreeing well with the expectations, but the downstroke motion providing very different results. No flow separation occurred, meaning no loop was verified for both C_l, C_d and C_m. The downstroke values are all higher than the values for the upstroke motion.

All the obtained results from dynamic simulations indicate major differences between dynamic stall and static stall. Each case of stall (light and deep) and each parameter (κ and Re) have singular characteristics that make the study of dynamic stall challenging and interesting. This study allowed to understand that dynamic stall does indeed provide the airfoil extra lift and stall does only occur at higher AoA. If the maximum AoA attained can be controlled, the helicopter have some extra-lift. However, this lift overshoot come at a cost: increased drag and strong nose-down pitching moment.

This work provided the values of aerodynamic coefficients for various cases. Converting these results in terms of power and thrust and compare them for a static stall case vs dynamic stall case is an interesting option for the future. In fact, this work's results indicate that neglecting dynamic stall is not possible, dynamic stall is present and is important. But what effect does it have not only in terms of aerodynamic coefficients, but in terms of power? The author hopes this work is used as a comparison for future works in dynamic stall.

6.2 Future work

Even though the objectives of the present project were met and most of the results are promising, some suggestions regarding improvements that ultimately might lead to better results are made.

The dynamic stall simulation performed used a medium mesh, with 3.5 million cells, a first suggestion to repeat the same simulation with finer meshes is made. Vortex shedding is a very important phenomenon when studying dynamic stall, reason why a finer mesh might lead to better results, due to better modelling of the vortices. This would also allow to conclude if a medium mesh, which is less demanding computationally, can be used to study such phenomena.

Furthermore, incompressible flow model was used. This, as referred to previously, reduces not only range of Re possible to be correctly simulated. High Re require high flow velocity, which, at high AoA, leads to transonic flow or even sonic flow at the LE of the airfoil. Such cases should be modelled with compressible flow models. In spite of this, first results were obtained for dynamic stall at high Re and those results should be used as a first comparison. In addition, using compressible flow model would also allow to study the influence of M_∞ on dynamic stall.

The method used in CFD simulations did not allow to simulate cases where α would be smaller than zero. Simulations with overset meshes might also be an interesting option. In those cases, the airfoil is the one governed by the pitching motion equation (as the real case). This broadens the range of motions possible to be study.

A helicopter blade in real flight not only suffers from pitching, but also from plunging. Studies comparing the development of dynamic stall with pitching, plunging and pitching plus plunging might also be of interest. Moreover, real flight is not 2D. CFD simulations for 3D cases, might also be interesting.

Lastly, past thesis' works on stall have developed *MATLAB* programs that reads files with the aerodynamic coefficients and returns the user the thrust and total power of the helicopter. Adapting those programs to dynamic stall (allow to read a hysteresis instead of a typical static stall curve) gives concrete results on the influence of dynamic stall on the performance of a helicopter. Some work has been done by the author to adapt it to dynamic stall conditions, although not completed, reason why such results were not presented in this work.

References

[1] W. McCroskey, “The Phenomenon of Dynamic Stall,” *NASA TM-81264,* 1981.

[2] V. d. Brederode, Aerodinâmica Incompressível: Fundamentos, 1ª ed., IST Press, 2014.

[3] J. G. Leishman, Principles of Helicopter Aerodynamics, 2nd ed., Cambridge University Press, 2006.

[4] D. McCormick, T. Anderson, B. Wake and D. MacMartin, “Rotorcraft Retreating Blade Stall Control,” *AIAA,* 2000.

[5] F. Gustafson and A. Gessow, “Effect of Blade Stalling on the Efficiency of a Helicopter Rotor as Measured in Flight,” *NACA Technical Note 1250,* 1947.

[6] M. Kramer, “Increase in the maximum lift of an airfoil due to a sudden increase in its effective angle of attack resulting from a gust,” *NASA TM-678,* 1932.

[7] R. Halfman, “Evaluation of high angle of attack aerodynamic derivative data and stall flutter prediction techniques,” *NACA TN 25433,* 1951.

[8] F. Sisto, “Stall-Flutter in cascades,” *Journal of Aeronautical Sciences,* p. Vol 20, 1953.

[9] A. Rainey, “Measurement of aerodynamic forces for various mean angles of attack on an airfoil oscillating in pitch and on two finite-spin weings osccilating in bending with emphasis on damping in the stall,” *NACA TR 1305,* 1957.

[10] N. Ham, “Aerodynamic loading on a two-dimensional airfoil during dynamic stall,” *AIAA Journal,* pp. Vol.6, no.10, 1968.

[11] P. Crimi, “Analysis of stall flutter of a helicopter rotor blade,” *AIAA Paper no. 73-403,* 1973.

[12] F. Carta, “Prediction of rotor instability at high forward speeds,” *USAAVLABS TR-68-18C,* 1969.

[13] L. Ericson, “Unsteady airfoil stall,” *NASA CR-66787,* 1969.

[14] L. McCroskey, “Dynamic stall experiments on oscillating airfoils,” *AIAA Journal vol.14 no.1,* 1976.

[15] N. Ham, “A Stall Flutter Of Helicopter Rotor Blades.- A special case of the dynamic stall phenomenon,” 1967.

[16] L. Carr, “Dynamic Stall Progress in Analysis and Prediction,” *AIAA Paper 85-1769CP,* 1985.

[17] P. Freymuth, “Further experimental evidence of vortex splitting,” *JFM vol.152,* pp. 289-299, 1985.

[18] M. Koochesfahani and V. Smiljanovski, “Effect of Initial Accelaration on the Development of the Flow Fiels of an Airfoil Pitching at Constant Rate,” *AFOSR Workshop on Physics of Forces Unsteady Separation,* 1990.

[19] M. Acharya and M. Metwally, “The unsteady pressure field and vorticity production at the suction surface of a pitching airfoil,” *AFOSR Workshop on Physics of Forces Unsteady Separation,* 1990.

[20] W. McCroskey, K. McAlister and L. Carr, “Dynamic stall experiments on the NACA 0012 airfoil,” *NASA Technical Paper 1100,* 1978.

[21] W. Shyy, Y. Lian, J. Tang, D. Viieru and H. Liu, “Aerodynamics of low-Reynolds number flyers,” *Cambridge University Press,* 2007.

[22] U. Lindhe Norberg, “Structure, form and function of flight in engineering and the living worlds,” *J.Morphol 252,* 2002.

[23] G. B. McCullough and D. E. Gault, “Examples of Three Representative Types of Airfoil-Section Stall at Low Speed,” *NACA TN 2502,* 1951.

[24] S. Digavalli, “Dynamic Stall of a NACA 0012 Airfoil in Laminar Flow,” *PhD Thesis, MIT,* 1994.

[25] S. Gupta and J. Leishman, “Dynamic stall modelling of the S809 aerofoil and comparison with experiments,” *Wind Energy 9,* pp. 521-547, 2006.

[26] E. Jumper, S. Schreck and R. Dimmick, “Lift-curve characteristics for an airfoil pitching at constant rate,” *J.Aircr. 24,* pp. 680-687, 1987.

[27] R. Ramsay, M. Hoffman and G. Gregorek, “Effects of Grit Roughness and Pitch Oscillations on the S809 Airfoil,” *NREL/TP-442-7817,* 1995.

[28] A. Choudhry et al., “An insight into the dynamic stall lift characteristics,” *Experimental Thermal and Fluid Science,* 2014.

[29] M. Robinson and J. Wissler, “Pitch rate and Reynolds effects on a pitching rectangular wing,” *Proceedings of the 6th Applied Aerodynamics Conference,* AIAA 1988.

[30] P. Choudhhuri and D. Knight, “Effects of compressibility, pitch rate and Reynolds number on unsteady incipient leading-edge boundary layer separation over a pitching airfoil,” *J Fluid Mech,* pp. 195-217, 1996.

[31] M. Chandrasekhara, M. Wilder and L. Carr, “Reynolds Number Influence on 2-D Compressible Dynamic Stall,” *AIAA Paper 96-0073,* 1996.

[32] W. McCroskey et al., “Dynamic stall on Advanced Airfoil sections,” 1980.

[33] A. Golestani, M. Bonab and M. Soltani, “An experimental study of buffet detection on supercritical airfoils in transonic regime,” *Journal of Aerospace Engineering 229(2),* pp. 312-322, 2014.

[34] M. Gad-el-Hak and C. Ho, “Unsteady vortical flow around three-dimensional lifting surfaces,” *AIAA J.24,* 1986.

[35] R. Jones and D. Cohen, “Aerodynamics of wings at high speeds,” 1955.

[36] L. Richardson, “The Approximate Arithmetical Solution by Finite Differences of Physical Problems Insolving Differential Equations, with an Application to the Stresses in a Masonry Dam,” *Trans. R. Soc. London, Vol 210,* pp. 307-357, 1910.

[37] R. Courant, K. Friedrichs and H. Lewy, “Über die partiellen differezengleichungen der mathematischen physik,” *Matematische Annalen 100,* pp. 32-74, 1928.

[38] J. Charney, R. Fjørtoft and J. von Neumann, “Numerical integration of the Barotropic Vorticity Equation,” *Tellus,* pp. 237-254, 1950.

[39] B. Riemann, “Über die fortplanzung ebener luftwellen von endlicher schwingungsweite,” *Abhandlungen der Königlichen Gesellschaft der Wissenschaften zu Göttingen,* 1892.

[40] S. Pope, Turbulent flows, Cambridge University Press, 2000.

[41] P. Spalart, “Young-person’s guide to detached eddy simulation grids,” *Technical report, NASA,* 2001.

[42] F. Menter, “Zonal two-equation k-w turbulence model for aerodynamic flows,” *23rd Fluid Dynamics, Plasmadynamics and Lasers Conference,* 1993.

[43] F. Menter, “Two-equation eddy-viscosity turbulence models for engineering applications,” *AiAA Journal,32(8),* pp. 1598-1605, 1994.

[44] J. Ekaterinaris and M. Platzer, “Computational prediction of airfoil dynamic stall,” *Prog. Aerospa. Sci. 33,* pp. 759-846, 1998.

[45] O. Reynolds, “On the dynamical theory of incompressible viscous fluids and the determination of the criterion,” *Philosophical Transactions of the Royal Society of London A.,* pp. 123-164, 1895.

[46] J. Boussinesq, Essai sur la théorie des eaux courantes, 1877, pp. 1-680.

[47] B. Launder and D. Spalding, “The Numerical Computation of Methods in Applied Mechanics and Engineering,” pp. 269-289, 1974.

[48] F. Menter, R. Langtry, S. Likki, Y. Suzen, P. Huang and S. Völker, “A correlation-based transition model using local variables - part i: model formulations,” *Journal of turbomachinery. 128(3),* pp. 413-422, 2006.

[49] R. Langtry and F. Menter, “Correlation-based transition modelling for unstructured parallelized computational fluid dynamics codes,” *AIAA journal 47(12),* pp. 2894-2906, 2009.

[50] P. Spalart and C. Rumsey, “Effective Inflow Conditions for Turbulence Models in Aerodynamic Calculations”.

[51] C. L. Ladson, “Effects of Independent Variation of Mach and Reynolds Numbers on the Low-Speed Aerodynamic Characteristics of the NACA 0012 Airfoil Sections,” *NASA TM-4074,* October 1988.

[52] L. Eça and M. Hoekstra, “A procedure for the estimation of the numerical uncertainty of CFD calculations based on grid refinement studies,” *Journal of Computational Physics 262,* pp. 104-130, 2014.

[53] L. Carr, “Progress in analysis and prediction of dynamic stall,” *J Aircr 25,* pp. 1-25.

[54] R. Green and R. Galbraith, “Dynamic recovery to fully attached aerofoil flow from deep stall,” *AIAA Journal 33(8),* pp. 1433-1440, 1995.

[55] S. Wang, D. Ingham, L. Ma, M. Pourkashanian and Z. Tao, “Numerical investigations on dynamic stall of low Reynolds number flow around oscillating airfoils,” *Computers&Fluids 39,* pp. 1529-1541, 2010.

[56] K. McAlister, S. Pucci, W. McCroskey and L. Carr, “An Experimental Study of Dynamic Stall on Advanced Airfoil sections Volume 2. Pressure and Force data,” *NASA Technical Memorandum 84245,* 1982.

[57] R. Prouty, “Helicopter Performance, Stability and Control,” *PWS Engineering Boston,* 2005.

[58] M. Mcveigh and E. Kisielowski, “A design summary of stall characteristics of straight wing aircraft,” *NASA Technical Report,* 1971.

[59] A. Spentzos et al, “Investigation of Three-Dimensional Dynamic Stall Using Computational Fluid Dynamics,” *AIAA Journal, Vol 43, No.5,* 2005.